Shear-wave velocity structure beneath the Dinarides from the inversion of Rayleigh-wave dispersion

Preprint *in* Earth and Planetary Sciences Letters · November 2020

DOI: 10.1016/j.epsl.2020.116686

4 authors, including:

Tena Belinić Topić
University of Zagreb
8 PUBLICATIONS **31** CITATIONS

SEE PROFILE

Josip Stipčević
University of Zagreb
40 PUBLICATIONS **329** CITATIONS

SEE PROFILE

Shear-wave velocity structure beneath the Dinarides from the inversion of Rayleigh-wave dispersion

Tena Belinić[a], Petr Kolínský[b], Josip Stipčević*[c] and the AlpArray Working Group[d]

Abstract

The interaction between the Adriatic microplate (Adria) and Eurasia is the main driving factor in the central Mediterranean tectonics. Their interplay has shaped the geodynamics of the whole region and formed several mountain belts including Alps, Dinarides and Apennines. Among these, Dinarides are the least investigated and little is known about the underlying geodynamic processes. There are numerous open questions about the current state of interaction between Adria and Eurasia under the Dinaric domain. One of the most interesting is the nature of lithospheric underthrusting of Adriatic plate, e.g. length of the slab or varying slab disposition along the orogen. Previous investigations have found a low-velocity zone in the uppermost mantle under the northern-central Dinarides which was interpreted as a slab gap. Conversely, several newer studies have indicated the presence of the continuous slab under the Dinarides with no trace of the low velocity zone.

Thus, to investigate the Dinaric mantle structure further, we use regional-to-teleseismic surface-wave records from 98 seismic stations in the wider Dinarides region to create a 3D shear-wave velocity model. More precisely, a two-station method is used to extract Rayleigh-wave phase velocity while tomography and 1D inversion of the phase velocity are employed to map the depth dependent shear-wave velocity. Resulting velocity model reveals a robust high-velocity anomaly present under the whole Dinarides, reaching the depths of 160 km in the north to more than 200 km under southern Dinarides. These results do not agree with

most of the previous investigations and show continuous underthrusting of the Adriatic lithosphere under Europe along the whole Dinaric region. The geometry of the down-going slab varies from the deeper slab in the north and south to the shallower underthrusting in the center. On-top of both north and south slabs there is a low-velocity wedge indicating lithospheric delamination which could explain the 200 km deep high-velocity body existing under the southern Dinarides.

Keywords: surface waves, Dinarides, collision, lithosphere

1. Introduction

The Mediterranean is one of the geologically most complex areas in the world. Tectonic evolution of this region has roots in the ongoing convergence between Eurasian and African plates that started in the Jurassic. Wedged between these two larger plates is the Adriatic microplate (Adria) which originated as a part of Africa that separated from the main continental body in the late Triassic - early Jurassic (Schmid et al., 2008 with references; Schmid et al., 2020). Adria played a pivotal role in the formation of the Mediterranean basin and surrounding orogens and in this process most of Adria was consumed either through collision or subduction processes (Ustaszewski et. al., 2010 with references; Handy et al., 2015; van Hinsbergen et al. 2019 and references therein; Schmid et al., 2020). Today, accreted remnants of Adria can be seen throughout the central and eastern part of the Mediterranean embedded in multitudes of mountain chains marking the northern margin of the wide Eurasian-African convergence zone (Handy et al., 2015; Schmid et al., 2020). Only part of the original "undeformed" Adria still visible at the surface is located under the Adriatic Sea and adjacent coastal areas (Fig 1.). Remaining Adriatic microplate is surrounded

on four sides with collision/subduction zones: Apennines to the west, Alps to the north, Dinarides to the east and Albanides-Hellenides to the south. For decades, regional studies were focused mainly on the northern and the western Adria margins while the southern and eastern ones were poorly explored; resulting in only a partial understanding of Adriatic mantle dynamics and its contribution to surface deformation and kinematics. Over the last ten years this began to change as the focus of the geophysical community slowly shifted to eastern side of the Adriatic Sea. This resulted in a number of investigations dealing with the evolution of the Dinarides and its role in the development of the central Mediterranean, both from the seismological and geological perspectives (e.g. Ustazewski et al. 2008, Šumanovac et al. 2009, Brückl et al. 2010, Stipčević et al. 2011, Handy et al. 2015, Šumanovac et al. 2017, Belinić et al. 2018). Although the newly sparked interest in the Dinarides provided valuable new results, only a handful of these were about the regional mantle structure leaving the question about the geodynamic driving forces unanswered.

The main aim of this study is to investigate the S-wave velocity in the uppermost mantle under the wider Dinarides region and interpret these findings in the context of regional geodynamics. Furthermore, by analyzing the velocity anomalies in the uppermost mantle we hope to identify distinct forces that shaped the Dinarides. For this purpose, we use a Rayleigh-wave tomography complemented by the 1D depth inversion of the surface wave phase velocity to create a regional 3D shear wave velocity model. These results provide valuable insight into the uppermost mantle structure linking the mantle dynamics with surface deformations.

2. Tectonic setting and mantle structure

The Dinarides are SW-vergent fold-and-thrust belt located on the NE Adriatic coast and extending from the Southern Alps in the northwest to the Albanides/Hellenides in the southeast. To the northeast, they are bounded by the Pannonian basin with a relatively wide transition zone in-between (Šumanovac et al., 2009). Their formation began with the north-east movement of the Adria and the progressive closure of the Neotethyan ocean in Middle-Late Jurassic (Pamić et al., 1998; Schmid et al., 2008; Handy et al., 2015). The subduction of the oceanic parts of Adria lasted till the early Paleogene when the shortening eventually reached the Adriatic carbonate platform and the process evolved to a collision (Tari 2002, Ustaszewski et al., 2010). Thrusting gradually migrated from northeast to southwest and in the process the outer parts of Adria were imbricated and overthrusted, creating a thick carbonate nappe pile whose thickness at some places exceeds 10 km (Aljinović, 1983). The Dinaric structures were also affected by the active extension in the Pannonian Basin initiated by the eastward lateral extrusion from the Alpine region which was followed by the subduction beneath the Carpathians (Royden and Horváth, 1988; Frisch et al., 1998; Horváth et al., 2006; Schmid et al., 2008; Vlahović et al., 2005). Furthermore, backarc extension in the Pannonian basin was accompanied by thinning of the lithosphere and influx of the hotter material from the asthenosphere affecting the mantle geodynamics in the Dinarides (Ustaszewski et al., 2010; Matenco & Radivojević, 2012; Handy et al., 2015). After cessation of the extension processes in the Late Miocene the Internal Dinarides were once again exposed to the contraction due to the translation and counterclockwise rotation of Adria (Anderson & Jackson 1987, Grenerczy et al., 2005; Vrabec et al., 2006, Bennett et al., 2008). At present, the Adria–Eurasian convergence is still ongoing across the eastern Adriatic-

Dinarides region and it is mostly accommodated by thrusting and strike-slip faulting within the external Dinarides (van Unen et al., 2018).

Despite the relatively well-established tectonic setting of the region, the underlying mantle structure is still not resolved in a satisfactory way and many open questions remain. Body wave tomography studies indicate a low-velocity anomaly beneath the northern-central part of the Dinarides, interpreted as a "slab gap" extending from the Eastern Alps to the Central Dinarides (Bijwaard and Spakman, 2000; Wortel and Spakman, 2000; Lippitsch et al., 2003; Piromallo and Morelli, 2003; Koulakov et al., 2009). The location of the slab gap is quite unexpected, considering the significant amount of shortening recorded in the upper crust along the whole Dinaric chain (Ustaszewski et al., 2008). In order to explain the slab gap, Ustaszewski et al. (2008) suggested that the asthenospheric upwelling due to the opening of the Pannonian basin thermally eroded the Adriatic lithospheric slab underthrusting the northern Dinarides. On the contrary, Handy et al. (2015) speculate that the mechanism responsible for the slab removal beneath the northern Dinarides is slab tearing. Furthermore, Handy et al. (2019) suggest that the slab break-off was initiated in Paleogene due to the southeast propagation of a subhorizontal tear beneath the Dinarides and propose that the slab tearing accumulated a downward pull on the still-attached slab beneath the Hellenides and triggered clockwise bending of the Dinarides-Hellenides chain.

Figure 1: Map of seismic stations used in this study (red triangles) overlaid on the regional tectonic map (modified from Schmid et al., 2008). Solid red lines represent main Tertiary faults, while the black barbed line defines the current orogenic front on the east Adriatic side.

Whereas the previous tomography results indicate lower velocity in the mantle under the northwestern Dinarides, the same investigations map a high-velocity anomaly reaching up to 200 km depth beneath the central and southern Dinarides (Bijwaard and Spakman, 2000;

Wortel and Spakman, 2000; Piromallo and Morelli, 2003; Koulakov et al., 2009, Zhu et al., 2012). Most authors see this high velocity body located west of the presumed Adria-Eurasia plate boundary as the subducting continental Adria lithosphere (Ustaszewski et al., 2008, 2010; Schmid et al., 2008; Handy et al., 2015; Šumanovac, 2015). Schefer et al. (2011) and Matenco and Radivojevic (2012) suggest lithospheric delamination and Dinaric slab rollback as a mechanism to explain westward shift of the high velocity anomaly in regards to the location of the oceanic suture zone (Sava zone). Furthermore, they also concluded that the same process is at least partially responsible for the extension in the south-eastern Pannonian basin and Internal Dinarides. Although most investigations agree on the changing nature of the interaction between Adriatic microplate and European mainland under the Dinarides, several studies have recently suggested that there is no discontinuation of the high-velocity zone below the NW Dinarides (Šumanovac and Dudjak, 2016; Šumanovac et al., 2017). Furthermore, both of these investigations have mapped deep reaching lithospheric slab extending up to 400 km depth. Recent S-receiver function study by Belinić et al. (2018) mapped thicker lithosphere beneath the NW and southern Dinarides (~110 km and ~90 km respectively) with an abrupt transition towards a significantly thinner lithosphere under the central Dinarides region (50-60 km) and the Pannonian Basin (60-70 km). This study aims to extend the research of uppermost mantle structure under the wider Dinarides region by using the new surface wave dataset and building on the previous work.

3. Data and method

Horizontally propagating surface waves are sensitive to lateral variations of the medium. Surface-wave phase velocities measured between two stations allow us to investigate the structure between the stations using long waves produced by distant earthquakes. Due to

the fact that longer periods sample larger depths, information about lateral velocity variations can be obtained over a large range of depths depending on the used period range. Moreover, in contrast to the subvertically propagating body waves, where the information is obtained only beneath the seismic station, the horizontal propagation allows us to study regions with low or uneven station distribution, as raypaths only need to cross the investigated region.

Over 40,000 waveforms from 98 seismic stations distributed in the wider Dinarides region including stations around the Adriatic Sea (Fig. 1) were collected. Most of the stations belong to the Croatian Seismic Network (CSN) and the Slovenian Environment Agency (ARSO), specifically 29 and 23, with 19 additional stations coming from the Italian National Seismic Network, 9 from the AlpArray temporary network (Molinari et al., 2016), 6 from the Hungarian National Seismological Network, 5 from the Mediterranean Network (MedNet), 5 from the Serbian Network of Seismic Stations, 1 from the Montenegro Seismological Observatory and 1 from the Albanian Seismological Network.

We analyzed 597 regional-to-teleseismic earthquakes recorded in the period from the beginning of 2010 till June 2018 with magnitude (Mw) greater than 6.0. The information about the earthquake origin time, location and magnitude were obtained from the ANSS Comprehensive Earthquake Catalog. The epicentral distances of the recorded events range from 20º to 120º to avoid near-source effects and interference from higher modes of Rayleigh waves. Total of 151 events yielded stable phase-velocity dispersion curves. Most of the events are located in the Pacific seismic zone stretching from Chile to Japan, which results in reduced sampling from the south-east (Fig. 2a).

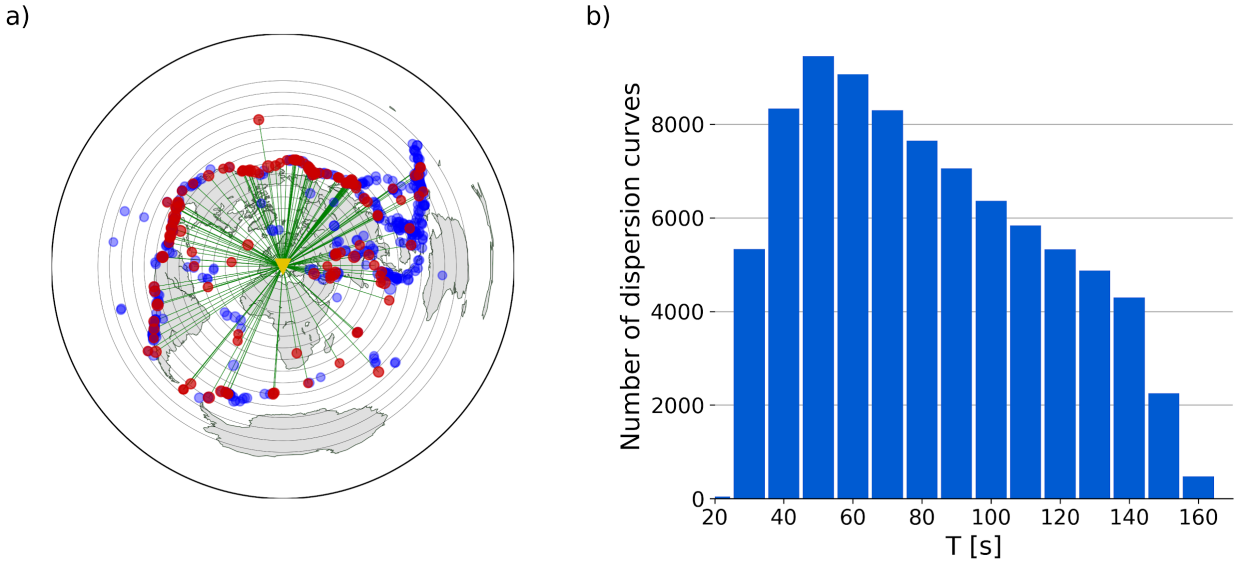

Figure 2: a) Map of earthquake locations used in this study (red dots mark used events, blue dots mark rejected events). Green lines are great circle paths, grey circles are n*1000 km distances and a yellow triangle marks the investigated region. b) Histogram of the number of good phase dispersion curves per period after applying the traveltime and smoothness criteria.

Following Kolínský et al. (2011), a two-station method is used to determine phase velocity of the Rayleigh waves recorded on the Z and R components. We start by multiple filtering of each record. This is done in the frequency domain and applied filters have non-constant relative resolution with filter width linearly depending on the period. Filtered spectra are then transformed back to the time domain resulting in a set of quasiharmonic signals and the local maxima of envelopes of these filtered signals is used to identify the fundamental mode. Group velocity dispersion curve is defined with the continuity criterion – a smooth curve in the spectrogram regardless of the absolute amplitude. Each narrow-band filtered signal is tapered in the time domain around the selected local maxima (group arrival time) to keep only the fundamental mode. The same width of filters in the frequency domain, as well as the same length of tapering in the time domain, is used for all records of a particular event to ensure the coherency of the records. Thus, for each station, a set of filtered records was assembled in both time and frequency domains.

To remove measurements affected by possible timing issues, only records where phase traveltime differs less than 6 s from the mean traveltime of all stations were kept. The amplitude zero crossings of the 50 s harmonic component were used to pick phase traveltime of each record. Typical profile length of interest is around 400 km for which the defined range of ± 6 s allows the path-averaged heterogeneity to be ± 6% (as the phase velocity of 50 s wave is around 4.0 km/s), while the localized heterogeneities smaller than profile length can still be larger than ± 6%. With those criteria only the outlying records with wrong timing were removed and records carrying information on the heterogeneity of the structure were kept.

Because the two-station method assumes a straight ray propagation, the station pair used to calculate phase velocity and the earthquake location have to be on the same great circle path. To ensure this, criteria set by Yao et al. (2006) were applied. For each event, we calculate two deviation angles α and β, where α is the azimuthal difference of the earthquake to the two stations and β is the azimuthal difference between the earthquake to the nearest station and the nearest station to the further station (see figure 12. in Yao et al., 2006). Stations are defined to be on the same great circle path if $\alpha < 5º$ and $\beta < 5º$. Also, to ensure reliable measurements at longer periods, we require that the interstation distance has to be larger than 100 km (Foster et al., 2014).

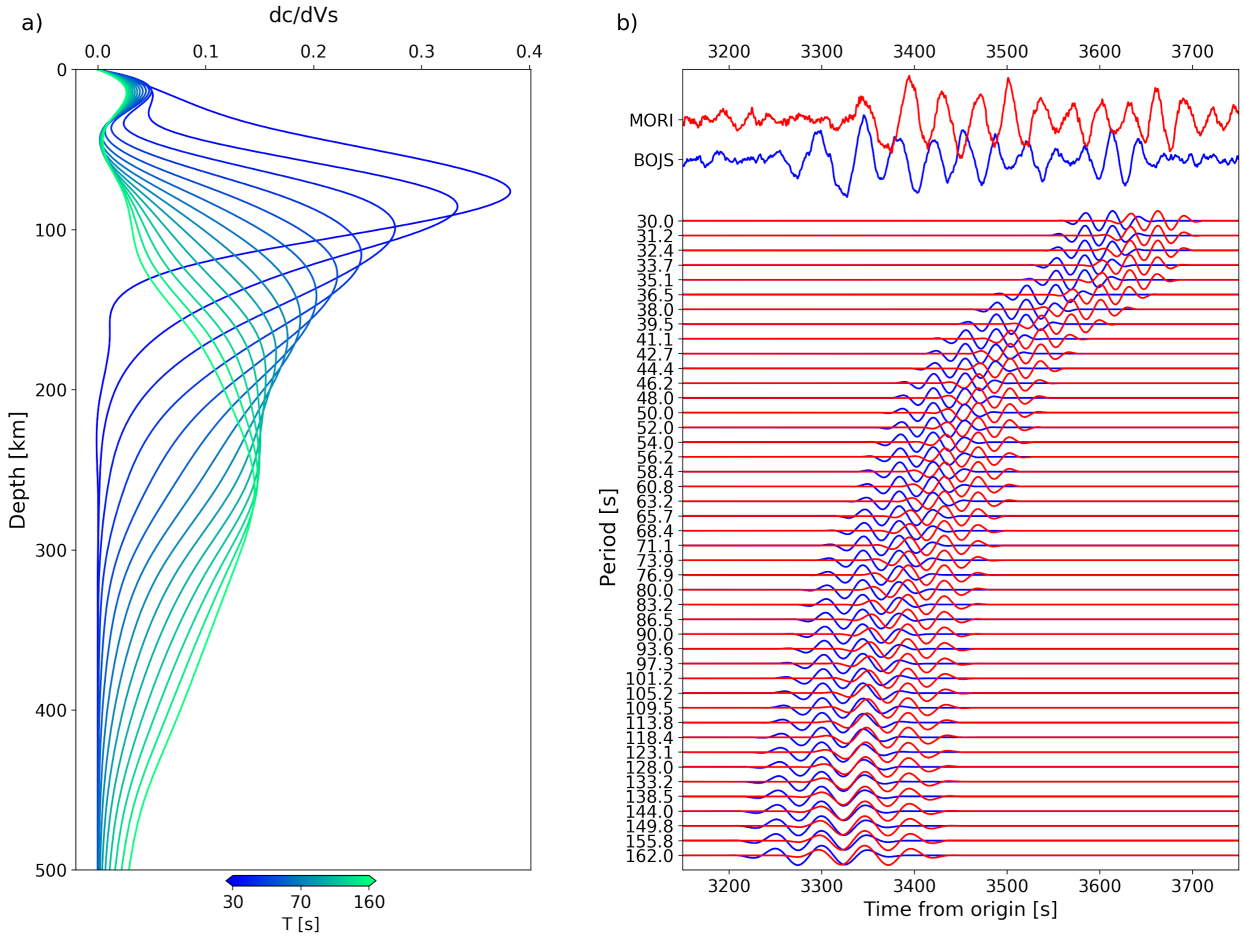

Figure 3: a) Depth sensitivity kernels for model ak135 of the Rayleigh wave for periods between 30 and 160s b) Quasi-harmonic signals of the event that occurred on 2018 May 4 at 22:32:54 GMT near Hawaii. The blue traces are recorded at the station BOJS and the red ones at the station MORI. Top panel shows raw seismograms. Central panel shows 27 traces bandpass filtered in the frequency domain at the periods shown on the left side and tapered in the time domain around the arrival time of the fundamental mode.

Finally, we cross-correlate the filtered and tapered quasi-harmonic signals measured at two stations to obtain the phase velocity dispersion. The dispersion curves were kept if their roughness is less than 0.1 km/s^2 (i.e. if the curve does not have large velocity jumps between two subsequent periods) and if the velocity differs less than 10% from the reference dispersion curve of the ak135 model (Kennett et al., 1995). Additionally, we keep the phase velocity curves only if both Z and R components of one station pair for a specific event satisfy

all previous criteria. Otherwise, we remove the dispersion curve from the dataset. For each station pair, we calculate the mean phase velocity dispersion curve by averaging all measurements for a given pair. The obtained phase velocity measurements have periods in the range from 30 s to 160 s. The low period limit is given by the teleseismic events used: shorter surface waves are much more attenuated and scattered and it is difficult to identify the fundamental modes for shorter periods coming from greater distances. The long period limit is given both by the earthquakes used (most of them were not large enough to produce longer waves) as well as by the instrumentation available (most of the sensor have corner period below 120 s, many only 30 and 40 s, so 160 s is at the limit where the phases are still not distorted).

All path-averaged dispersion curves are inverted to obtain lateral variations of phase velocity for selected periods (phase-velocity maps). Tomography was calculated for 44 selected periods starting at the period of 30 s continuing with a multiplicative step of 1.04 between two consecutive period values up to the period of 162 s. The geometric sequence is used to resemble the period values obtained by multiple filtering. The bigger absolute difference between the values towards larger periods reflects the decreased sensitivity of longer waves. We use a 2D tomography method of Yanovskaya and Ditmar (1990), which has been widely applied (e.g. Ritzwoller and Levshin, 1998; Bourova et al., 2005; Raykova and Nikolova, 2007; Guidarelli et al., 2017). Tomographic inversion is done for the region defined by the latitudes [40º–48º] and longitudes [10º–22º] with a grid spacing of 0.1º. The regularization parameter value was set to 5.0, which produces relatively smooth phase velocity variations. The regularization parameter controls the trade-off between fitting the traveltime and smoothing of the resulting model. Lateral resolution of the phase velocity

distribution is given by an elliptical area which depends on the path density, azimuths and lengths. It is expressed by resolving factors L and ε where L is the size and ε is the stretching of the averaging area (Yanovskaya et al., 1998). Small values of L and ε ensure high lateral resolution. Smaller L means that the large number of paths are intersecting, while small ε (ε < 1) means that the paths are uniformly distributed with no preferred orientation. We consider the area as well resolved if L < 150 km for that region (see Fig. 4b). Comparisons performed by Ritzwoller and Levshin (1998), Fang et al. (2010) and Tondi et al. (2019) showed that the resolution estimates are the same using the checkerboard test and the averaging area. Hence, as pointed out by Panza et al. (2007), it is not necessary to perform the checkerboard test when using the resolution estimates based on the averaging area and stretching provided by the method of Yanovskaya at al. (1998).

Rayleigh wave phase-velocities for periods in the range from 30 s to 160 s are primarily sensitive to depths between 40 and 400 km and have a peak sensitivity between 80 and 250 km (Fig. 3, calculated using the code by Herrmann (2013) and model ak135 of Kennett et al. (1995)). The phase-velocity dispersion curves have been inverted at each node of the tomography grid for a 1D shear-wave velocity structure, by following the procedure described in Kolínský et al. (2014). For the inversion, we use the isometric method (Málek et al., 2007) where forward problem is solved by the modified Thomson-Haskell matrix method (Proskuryakova et al., 1981). Dispersion curves are found in a 1-D layered model above a halfspace while searching for values of v_S and v_P in the individual layers. We use 23 layers for the upper 300 km. Their thicknesses are generally increasing towards greater depths which corresponds to decreasing resolution capability of surface waves. The thicknesses are kept constant during the inversion. Below 300 km, the medium is considered as a halfspace.

Shear-wave velocities in the halfspace are found by the inversion the same way as in all the layers above. The longest waves used still have significant sensitivity for these depths (see Fig. 3a). Similarly, as in Kolínský et al. (2014), preliminary tests of different layer distributions were performed before the final inversion parametrization was selected. This resulted in a set of thinner layers around the Moho depths to allow the inversion to map the increased velocity gradient. Our aim is not to estimate the Moho depth - surface waves have limited ability to resolve precisely the depth of a boundary. Thinner layering around the Moho avoids possible unrealistic steps in the wrong depth, which could happen if only one boundary is prescribed around the Moho depth. The number of layers was also tested to be sufficient for imaging the structural variations. Higher number of layers do not bring any qualitative change of the resulting models (Kolínský et al., 2011), it only smears the velocity gradients over more thinner layers. The ak135 model is used to set the density and v_P/v_S ratio. Inversion of the dispersion results at each grid node is done in two steps. First, the average dispersion curve for the whole region is inverted, i.e. the mean value of all nodes at each period. The resulting best model is then used as a starting model for the inversion at all grid nodes. While the inversion does not depend on the starting model, using a model close to the final one saves computational time (Kolínský et al., 2011, 2014). Unrealistic velocity oscillations are avoided by constraining the velocity difference between neighboring layers. We allow for a step of +0.9 km/s and -0.15 km/s for each lower layer with respect to the previous one. We also made sure that our inversion results never reach these values. The constraints are used during the inversion to limit the range of velocities which are browsed for each layer, however, they are set so broad that the final model is not limited by them. Furthermore, we invert the phase velocity dispersion curve 30 times at each node. These 30 runs are used to map the nonuniqueness of the inversion. Each dispersion curve can be

explained by many models with almost the same misfit. Each inversion run consists of 5000 - 7000 iterations (one iteration means setting a new model, forward calculation and evaluation of the misfit). As the new models are produced using the previous models with random perturbation added for each iteration, each inversion run, in general, reaches another local minimum of the misfit function. The final shear-wave velocity structure is then calculated as the mean of all 30 models. Furthermore, tests were performed to confirm that the final mean model doesn't change if more than 30 individual models are used. The mean model differs qualitatively from all the individual 30 models. Although it does not necessarily have the lowest misfit, it usually has the lowest complexity. The complexity is measured as an average of absolute values of all the velocity steps between the layers normalized by the number of layers. Moreover, the product of the misfit and complexity is then by far much lower than the same measure of any of the 30 individual models. The mean model is the closest one to the unrealistic ideal point where both misfit and complexity are the lowest (see Fig. 11 in Kolínský et al., 2014). The low complexity of the mean model is a consequence of the way that model is calculated, not a criterion for selecting it. Besides, having 30 individual models not only allows us to calculate the mean model but also standard deviation of that model which is then used as a measure of the inversion uncertainty.

4. Results

The first step in the creation of the 3D shear-wave velocity model is to apply a tomography procedure to the path-averaged phase velocities for all available periods (30–160 s). Surface wave tomography results are shown in Fig. 4 as the period dependent phase velocity maps along with the resolution maps for representative periods (50, 100, and 150 s). Comparing Figs. 4a and 4b, it can be seen that the spatial resolution L is better in the areas that are more

densely covered by intersecting seismic paths. The best resolution is observed beneath the NW Dinarides with L < 50 km. The whole wider Dinaric area has a good resolution (mean averaging area L is mostly less than 100 km) for all considered periods, even for periods above 150 s, which implies that these tomography maps are appropriate for identifying structures with the size of 100 km and larger. The resolution becomes worse at the edges of the investigated area, where the path coverage is poor. The stretching of the averaging area ε mostly varies between 0 and 1 (Fig. 4c), except for parts of central and south Adriatic. The values of ε less than 1 indicate that the azimuthal path

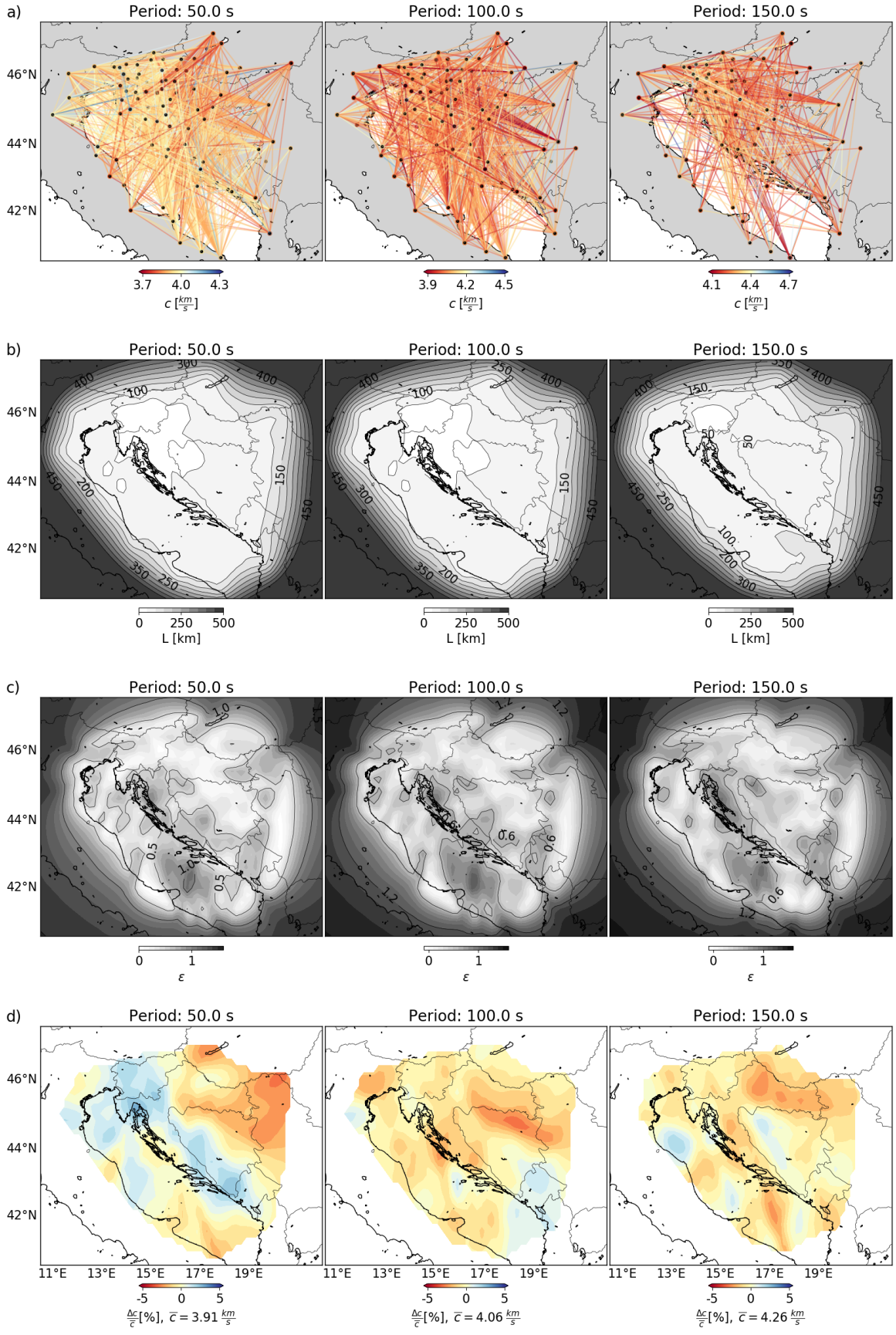
a)
Period: 50.0 s
Period: 100.0 s
Period: 150.0 s
46°N
44°N
42°N
3.7 4.0 4.3
c [km/s]
3.9 4.2 4.5
c [km/s]
4.1 4.4 4.7
c [km/s]
b)
Period: 50.0 s
Period: 100.0 s
Period: 150.0 s
0 250 500
L [km]
c)
Period: 50.0 s
Period: 100.0 s
Period: 150.0 s
0 1
ε
d)
Period: 50.0 s
Period: 100.0 s
Period: 150.0 s
11°E 13°E 15°E 17°E 19°E
-5 0 5
Δc/c̄ [%], c̄ = 3.91 km/s
Δc/c̄ [%], c̄ = 4.06 km/s
Δc/c̄ [%], c̄ = 4.26 km/s

Figure 4: For periods of 50, 100 and 150 s: a) the interstation path velocities (color marks velocity); b) and c) the resolution maps i.e. averaging area and the stretching factor calculated following Yanovskaya and Ditmar (1990); d) the phase velocity maps (only for areas with resolution L < 150 km).

distribution is sufficiently uniform and that the resolution is almost the same in any direction. Therefore, the high-density coverage of the interstation paths ensures sufficiently high-resolution beneath the wider Dinarides region for the whole period range.

Fig. 4d shows the phase velocity maps for the area with resolution L<150 km. Well defined slow-velocity anomaly coincides with the south-western part of the Pannonian basin for all periods, while a less pronounced slow-velocity anomaly dominates the central Adriatic-Dinarides region for periods longer than 50 s. Phase velocity map for the period of 50 s shows fast-velocity anomaly extending close to the Adriatic coast from the north-western to southern Dinarides. For longer periods, the fast-velocity region shifts further inland and becomes less pronounced with the exception of South Dinarides where it remains strong at all periods. In the central-southern Adriatic the SE-NW elongated low velocity area is present in all periods as can be seen in Fig. 4d. This elongation is probably due to a higher stretch of the averaging area (ε=1.2) as most of the paths in this area have SE-NW direction generating velocity smear along this course and resulting in vague and ambiguous interpretation (Fig. 4c). Nonetheless, this result indicates the existence of the low velocity anomaly under the central-southern Adriatic region, the exact shape and location of which will have to be mapped in the future investigations.

As the main focus of this research was to create a 3D shear-wave velocity model of the mantle structure, we inverted the phase velocity dispersion curves taken at each grid point from the previous step to determine the shear-wave velocity structure of the uppermost mantle. Fig.

5 shows the examples of 1D phase velocity inversion at three different geographic locations with markedly different tectonic setting: (a) Pannonian basin, (b) NW Dinarides and (c) southern Dinarides. In the rightmost column of the Fig. 5 are the results of the 1D phase velocity inversion with no additional lateral smoothing.

The lithosphere asthenosphere boundary (LAB) is usually defined as the middle depth of the depth range in which shear velocity decreases (Bartzsch et al., 2011). The models shown in Fig. 5 have a local minimum of shear-wave velocity beneath the Pannonian basin at the depth of 140 km, beneath NW Dinarides it is around 180 km, and about 200 km in the southern Dinarides. The NW Dinarides region has the most prominent velocity-depth variations, while beneath the Pannonian the low velocity zone is less pronounced. From this, we can see that the LAB is shallower under the Pannonian domain, deep in NW Dinarides and deepest in southern Dinarides. In addition to Fig. 5, two more examples of 1D structures in the region are given in Fig. A1. Our period range is sensitive mainly to the upper mantle structure, however, for all periods, there is always a non-zero sensitivity at crustal depths. Appendix A evaluates the influence of crustal layers on the depth inversion. Testing two crustal models we show that the resulting upper mantle structure does not depend on the crustal velocities.

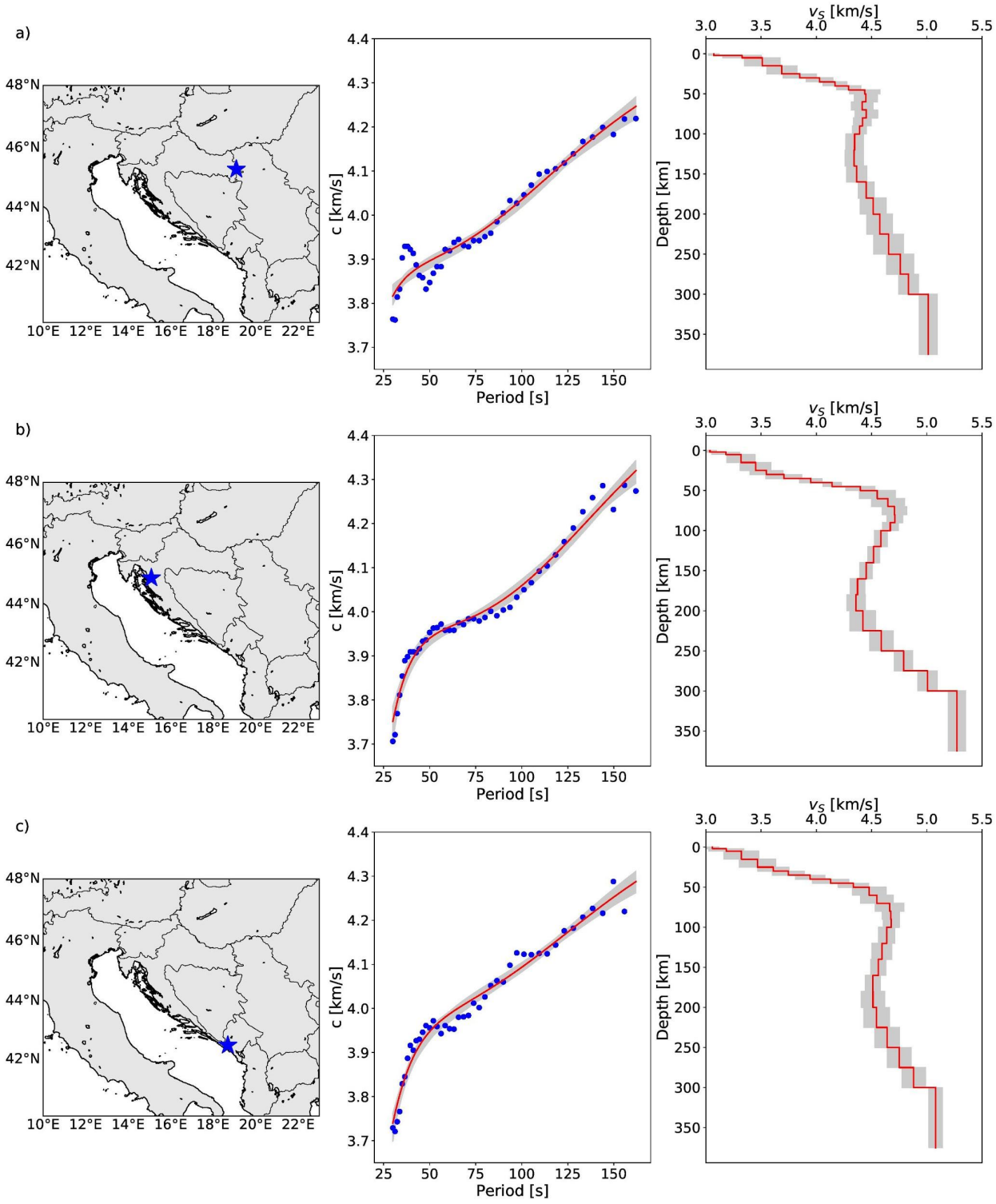

Figure 5. Example of the 1D phase velocity inversion for three different locations. Blue stars mark the location while the blue dots indicate the phase velocities taken at each location from the phase velocity maps. Red line in the same image is the dispersion curve of the final mean model with the variations between minimum and maximum velocity in grey. The rightmost panel shows the final mean shear-wave velocity structure (red line) obtained after 30

inversions. Grey area represents the standard deviation for each layer calculated from the 30 individual models.

Finally, as the main focus of our study is the regional shear wave velocity model previously calculated 1D models are interpolated and smoothed to create the 3D model. The results shown in Figs. 6 and 7 display shear wave velocity maps and vertical cross-sections. The maps shown in Fig. 6 display similar features as those observed in the phase velocity results. Low-velocity anomaly dominates the Pannonian basin at all depths, while the small region of higher velocity exists beneath the central Adriatic islands for depths larger than 120 km. The most striking feature is a high-velocity anomaly beneath the whole Dinarides, reaching a depth of more than 200 km in the southern portion of the investigated region (Fig. 6). The whole anomaly persists until depths of 140-160 km when it starts to fade beneath the central Dinarides but remains visible under the northern and southern part even at depths of 200 km (Fig. 6e, f). Furthermore, the high velocity anomaly changes the location with depth as it shifts from the Adriatic coast towards the Pannonian basin with increasing depth.

From cross-section shown in Fig. 7b, we see that the high-velocity zone is thinner beneath the central Dinarides and gets thicker towards the northwestern and southern Dinarides. Its upper boundary is shallow beneath the southern and central parts and deepens toward the north. There is a visible anomaly break towards Eastern Alps, but still, the high-velocity zone covers the entire Dinaric region. Taking a look at cross-sections perpendicular to the orogen (Figs. 7c–7j), a subducting high-velocity anomaly is seen following the front of the orogen. Going from the north to the south it becomes less steep but thicker, ranging from 60 km beneath NW Dinarides to 140 km beneath the southern Dinarides. Under the central part of the Dinarides, this shallow high-velocity anomaly is missing its deeper root and reaches a depth of 140 km (Fig. 7g), while beneath NW Dinarides its front is almost vertical (Fig. 7e).

On northern profiles (Fig. 7c–7f), the anomaly is unbroken beneath the whole Adriatic Sea while on southern profiles it separates into eastern and western parts (Fig. 7g–7j). From these results, it is clear that the aforementioned “slab gap” observed by teleseismic tomography under NW Dinarides isn't the result of the missing Adriatic lithosphere and it should be explained differently.

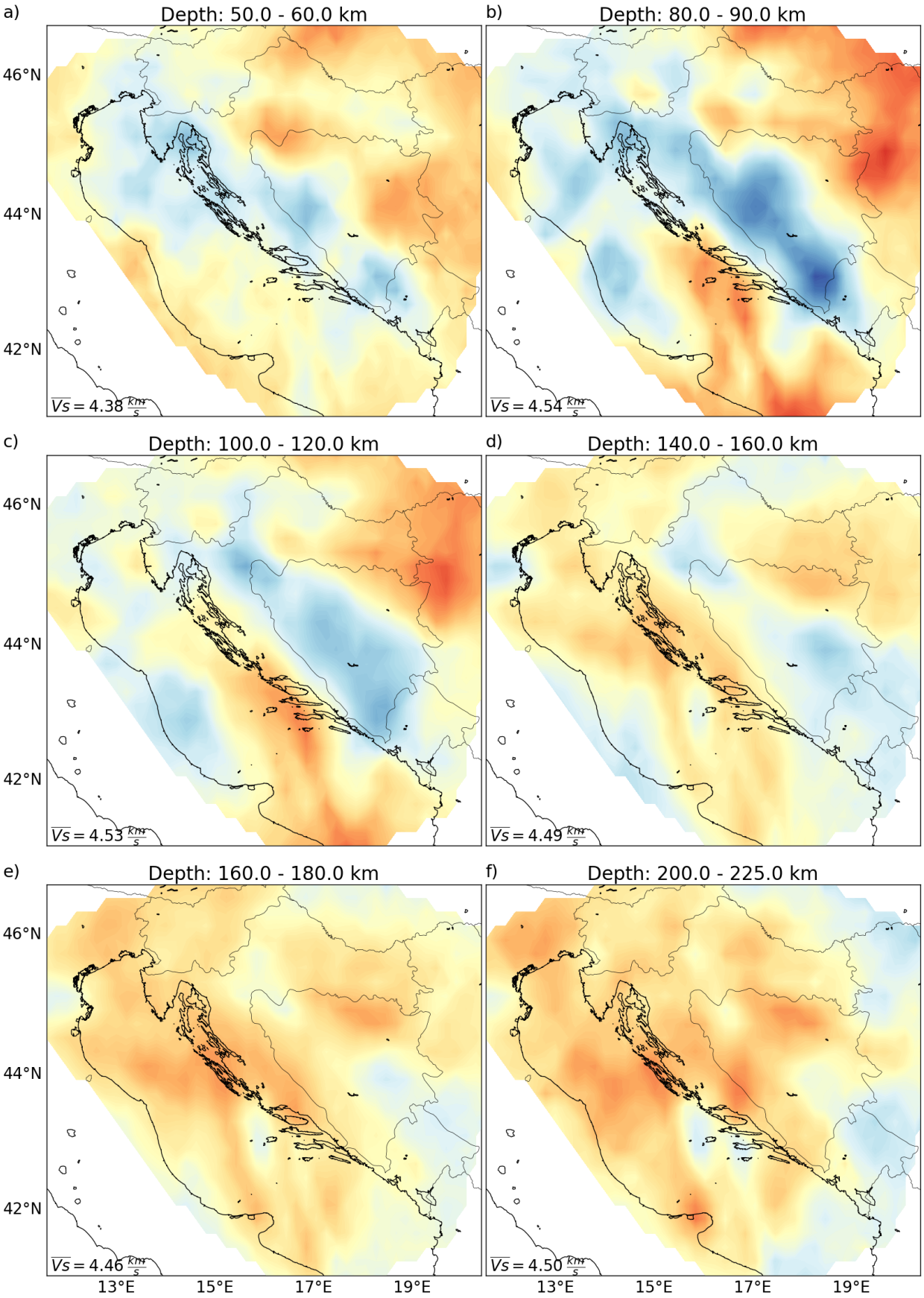
a)
Depth: 50.0 - 60.0 km
$\overline{Vs} = 4.38 \frac{km}{s}$
b)
Depth: 80.0 - 90.0 km
$\overline{Vs} = 4.54 \frac{km}{s}$
c)
Depth: 100.0 - 120.0 km
$\overline{Vs} = 4.53 \frac{km}{s}$
d)
Depth: 140.0 - 160.0 km
$\overline{Vs} = 4.49 \frac{km}{s}$
e)
Depth: 160.0 - 180.0 km
$\overline{Vs} = 4.46 \frac{km}{s}$
f)
Depth: 200.0 - 225.0 km
$\overline{Vs} = 4.50 \frac{km}{s}$
46°N
44°N
42°N
13°E
15°E
17°E
19°E
-10
0
10
$\frac{\Delta Vs}{\overline{Vs}}$ [%]

Figure 6. Maps of the shear wave velocity model obtained after the inversion of phase velocity dispersion curves for layers at depths: 50-60, 80-90, 100-120, 140-160, 160-180 and 200-225 km.

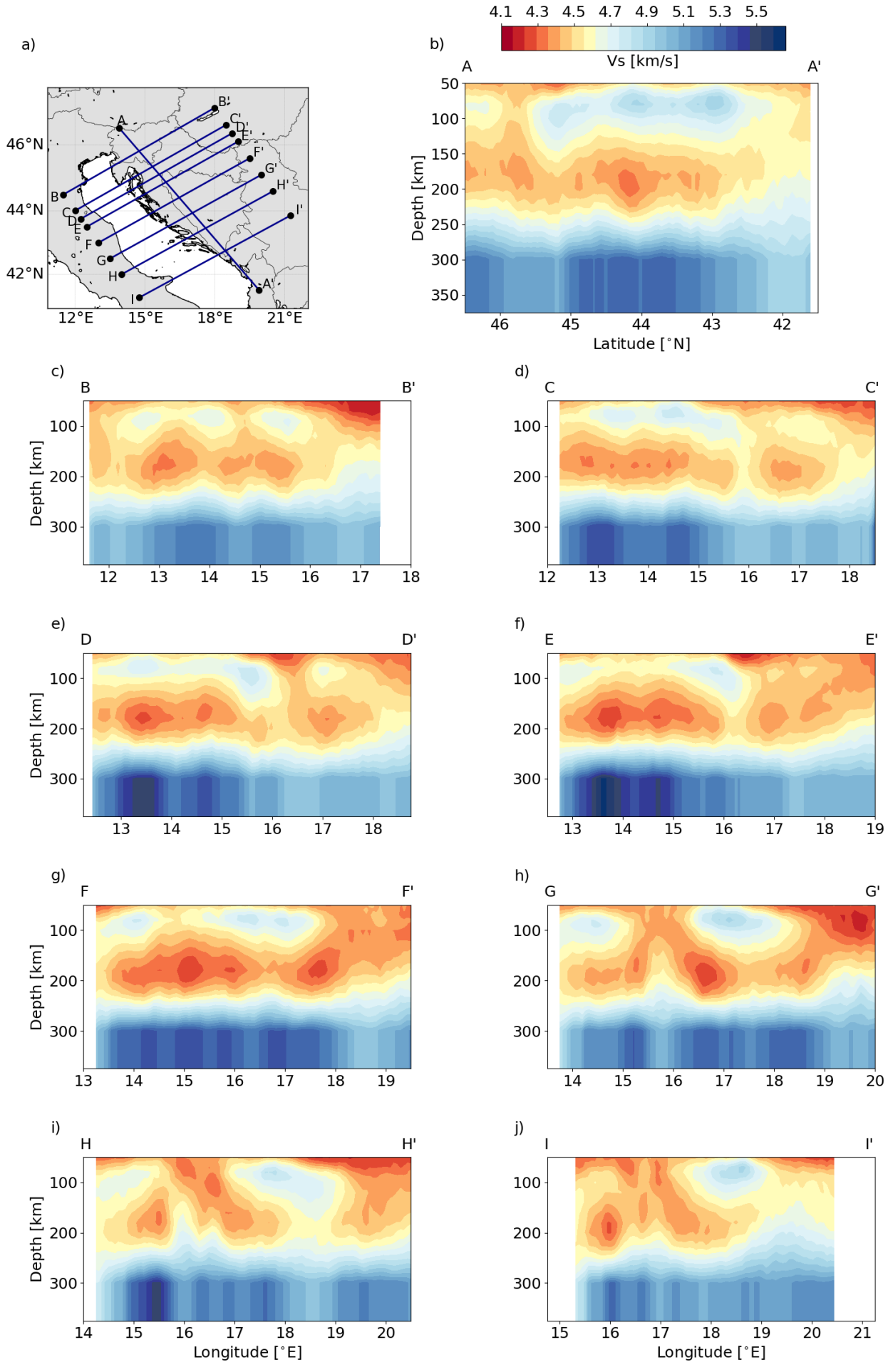
a)
46°N
44°N
42°N
12°E
15°E
18°E
21°E
A
A'
B
B'
C
C'
D
D'
E
E'
F
F'
G
G'
H
H'
I
I'
b)
4.1 4.3 4.5 4.7 4.9 5.1 5.3 5.5
Vs [km/s]
A
A'
Depth [km]
Latitude [°N]
c)
d)
e)
f)
g)
h)
i)
j)
Depth [km]
Longitude [°E]

Figure 7. Cross-sections through the shear wave velocity model. a) Location of the cross-sections shown in this figure. Please note that the depth of each profile starts at 50 km as we excluded the uppermost part where the surface waves have low sensitivity (see Appendix A). Panel b) shows the shear velocity versus depth in the upper mantle along the profile parallel to the Dinarides. Panels c) through j) show the shear velocity versus depth in the upper mantle along the profiles crossing the Dinarides.

5. Discussion

The uppermost mantle structure under the Dinarides is poorly known and most of what is known stemmes from the teleseismic body waves investigations and these are providing rather contradictory results. On one side the majority of the investigations were indicating a break in the high velocity body under the northwestern and central Dinarides interpreting this as the "slab gap" (Bijwaard and Spakman, 2000; Wortel and Spakman, 2000; Piromallo and Morelli, 2003; Koulakov et al., 2009; Mitterbauer et al., 2011) while others were mapping continuous slab under the same area (e.g. Šumanovac, 2015; Šumanovac and Dudjak, 2016). Recently, a couple of papers were published that seemed to confirm the commonly accepted view of "slab gap" (Šumanovac et al. 2017, Belinić et al., 2018) but both indicated significantly more complex disposition of the lithosphere under this region. Using S-wave receiver functions Belinić et al. (2018) mapped thinned lithosphere at the transition between the northwestern and central Dinarides corroborating the "slab gap" influenced geodynamic models of Ustaszewski et al. (2008) and Handy et al. (2015). On the other hand, that research hinted that the mechanism to explain thinned lithosphere lies in the lithospheric delamination process. Similarly, the results from the work of Šumanovac et al. (2017) indicate the break in the high velocity body under the same region but only for the deep reaching slab whereas the shallower part of the slab (<100 km) remains continuous along the entire Dinarides area.

Common to all these investigations was the use of teleseismic body waves of limited spatial and depth resolution thus extrapolating features in the lithosphere that were not realistic or even skipping some of the more intricate structural details. To bridge this gap, we used surface waves from a large number of regional and teleseismic events in combination with the two-station method thus significantly improving both spatial and depth resolution (see resolution distribution in Fig. 4). By using surface waves of different periods (30 to 160s range) with different depth sensitivity we created the 3D shear velocity model shown in Fig. 6. The most robust feature in the shear velocity model is the high velocity anomaly present under the whole Dinarides range, reaching depths of 160 to more than 200 km going from north to south (Fig. 6). This result is in sharp contrast with most of the previous investigations which show shallow high velocity anomalies under the north-western and central-southern Dinarides with a clear transition zone of lower seismic velocity between them (Wortel, 2000; Piromallo and Morelli, 2003; Koulakov et al., 2009). As previously discussed this transition zone was interpreted as the slab gap and several hypotheses were suggested to explain it (Ustaszewski et al., 2008; Handy et al., 2015). On the contrary, our results show continuous underthrusting of the Adriatic lithosphere under Eurasia along the whole Dinarides region with notable variations in the geometry of the downgoing slab. This is in line with the findings of Šumanovac et al. (2017) although with some significant differences in both geometry and the depth of the slab. Furthermore, continuous shallow slab was also mapped in ambient noise tomography studies of Kästle et al. (2018, 2020).

In order to examine the structural variations, present in the new shear-wave model, more closely we draw several profiles along and across the Dinarides. The profiles and their

respective locations are shown in Fig. 7 and what is immediately visible is the variable disposition of the lithospheric high velocity anomaly (blue colors) in different parts of the Dinarides. From the profile AA' which runs along the Dinarides it appears as if the Adriatic slab is deeper under the northern Dinarides than under their southern portion. This seems in opposition to the results presented in Fig. 6 where we clearly indicated that the slab depth is greatest in the south. The key to this conundrum lies in the profiles across the Dinarides (Figs. 7c–7j). These profiles show steeply inclined slab under the northwestern Dinarides reaching 150-160 km depth (profiles CC', DD' and EE') transforming to gently sloping high velocity body in the central Dinarides (profiles FF' and GG') with depth not exceeding 140 km and then again becoming more inclined under the south Dinarides with slab reaching depths of 180-200 km (profiles HH' and II'). Furthermore, the profile HH' shows that the southern portion of the Adria slab extends much further inland than its northern counterpart, becoming highly inclined only in the last section thus exacerbating the difference seen in profile AA'.

Combining all the results presented in the Figs. 6 and 7 we created a structural model of the uppermost mantle for the Dinaric convergent zone. The model, shown in Fig. 8 delineates two zones of deeper slabs in the north and south with shallower underthrusting lithosphere in-between. As discussed below we believe this model elegantly solves the apparent mismatch about the nature of the lithospheric velocity anomaly under the north-central Dinarides seen in various investigations previously mentioned. The central idea behind the model is the mechanism to explain both high and low seismic velocity anomalies under the same region. The shape and the geometry of the lithospheric high velocity body present in our results strongly support the idea of delamination and slab sinking under the northern

and southern portion of the Dinarides. This model was first proposed by Schefer et al. (2011) and Matenco and Radivojević (2012) as a mechanism to explain a 200 km deep high velocity body under the southern Dinarides. Building on this idea, Belinić et al. (2018) interpreted findings of thinned lithosphere under the north-central Dinarides in the context of delamination processes. On the other hand, Šumanovac and Dudjak (2016) reported the presence of the high velocity body steeply sloping to the east reaching depth of 200 km under that same area but also mapped a lower velocity body overlaying part of the slab (see their Fig. 10). Similarly, we image a low velocity wedge present on-top of both north and south slabs possibly indicating inflow of hotter asthenospheric material (see profiles BB' and DD' in Fig. 8). So, it is plausible that the reason for the missing slab in some of the teleseismic investigations is the hotter asthenospheric material partially masking the high velocity region along with the lower resolution in the regional-continent wide teleseismic tomography. Therefore, our results along with the input from previous investigations strongly favor the model incorporating delamination and sinking of the Adria mantle lithosphere under the northwestern and southern Dinarides with the hotter mantle material filling the space vacated by the sinking slabs. In this context it is also important to mention that in the model of Handy et al. (2015) the short slab is connected with the slab break-off in Oligocene. Our results strongly support this idea although the depth range in this investigation doesn't allow us to connect the short slab with a tear below.

Although the main aim of this research was to describe the uppermost mantle structure of the Dinaric collision zone, some of the surrounding regions were also mapped in the process. Part of the Pannonian basin covered by this research can be clearly seen in the results as the region of the lower seismic velocity in the northeastern corner of Fig. 6. This area of the

reduced velocity extends to depths of at least 150 km and is consistent with the upwelling of hot asthenospheric material triggered by the spreading in the Pannonian basin (e.g. Ustaszewski et al., 2008). Surprisingly, in the northwestern portion of the region encompassed by this research, more specifically in the area where Dinarides connect to the Southern Alps our results do not show the expected zone of thickened lithosphere. Whereas Belinić et al. (2018) mapped somewhat thicker lithosphere in the northwesternmost corner of the Dinarieds, ranging between 120 and 130 km, our results show clear interruption between deeper high velocity body under the north-central Dinarides and the shallower one located more to the north (see left side of the profile AA' in Fig. 7). On the other hand, using the Rayleigh waves (periods from 5s to 37s) extracted from ambient noise, Guidarelli et al. (2017) detected a region of the reduced velocity in the uppermost mantle closely aligning with results shown in our profile BB' in Fig. 7. Although the results shown in that profile indicate a higher velocity area reaching depth of 100 km, this anomaly is weak and localized. All this suggests that the lithospheric structure of this transition zone is much more complex than previously thought and requires more in-depth investigation. Most of what is assumed to be non-accreted remnants of Adria microplate (closely covering Adriatic Sea region) was also covered in this investigation although the results for that region are highly distorted due to the poor path coverage (see Fig. 4c). Nevertheless, there is a clear pattern emerging with a lower velocity region located in the central Adriatic dividing areas of higher velocity to the north and south of it. The area of lower velocity can be seen in all the profiles crossing the mid Adriatic zone, possibly pointing towards fragmentation of the Adria microplate but this has to be investigated further in the subsequent studies.

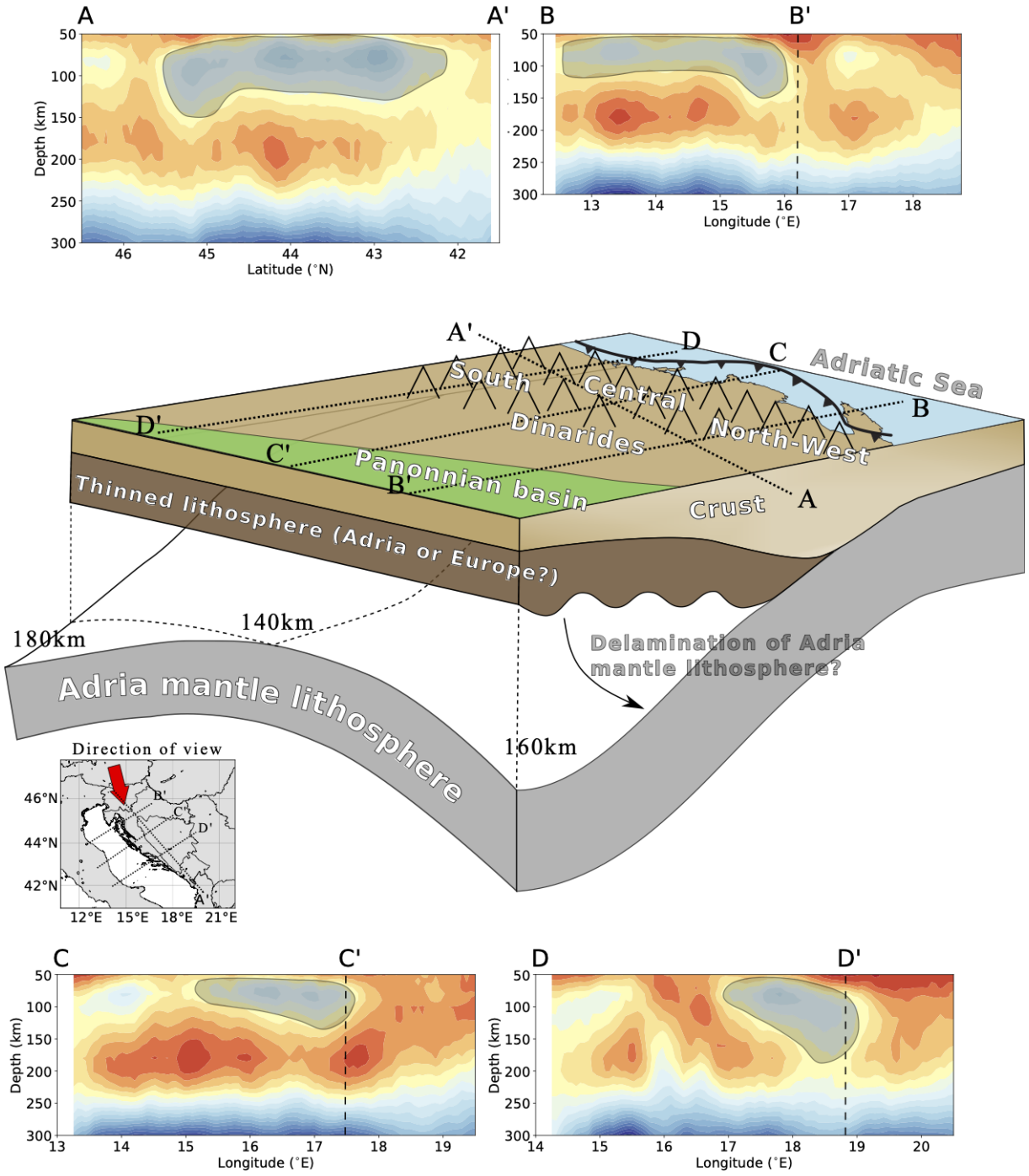

Figure 8. Schematic interpretation of the Dinarides lithospheric structure (not to scale) from the new 3-D shear-wave velocity model. Subimages a) to d) are the cross-sections through the new shear-wave velocity model with shaded areas marking the location and shape of the underthrusting Adriatic lithosphere (depth section starts at 50 km). Markings AA', BB', CC' and DD' denote the extent of the interpreted part of each cross-section in the main tectonic sketch. The locations of the cross-sections along with the view angle of the tectonic sketch are shown in a small subimage in the left corner of the

central panel. Tectonic sketch in the central image depicts the subducted Adria lithosphere beneath the Dinarides. The depth, extent and the geometry of the subducted lithosphere varies from north to south suggesting different mechanisms of slab creation. Dark brown color denotes the thinned lithosphere of uncertain origin, either thermo-chemically thinned European or possibly Adriatic, thinned due to delamination.

6. Conclusion

In this work we present the first 3D shear wave velocity model of the uppermost mantle for the wider Dinarides region. For this purpose, we collected recordings from a large number of seismic stations operating in the region thus allowing us to have excellent coverage for most of the Dinarides. The model was constructed using the arrival time measurements from recordings of regional-to-teleseismic surface waves on pairs of stations and employing the tomography on this data.

The results show a high velocity anomaly present under the whole Dinarides up to depths of 140 km with a clear break in the high velocity body when transitioning to the Alpine region. Higher velocity anomaly is significantly deeper in the south, reaching depths of 200 km at the southern edge of the Dinaric mountain chain. From the shear velocity model, it is clear that the nature of interaction between Adria and the Eurasian mainland varies significantly along the Dinarides. The geometry of the high velocity body indicates the possible delamination of the lithosphere under the north-central and southern Dinarides, transforming to underthrusting under the central part. Lower velocity areas present under the southwestern portion of the Pannonian basin and the central Adriatic Sea indicate lithospheric thinning and/or upwelling of the hotter asthenospheric material.

Acknowledgments

The authors thank Tatiana B. Yanovskaya for providing the surface-wave tomography code and for useful advice on how to use it. The study has been supported by the Croatian Science Foundation, grant HRZZ IP 2014-09-9666. The waveform data were provided by the following regional seismic networks: SL (Slovenian Environment Agency, 2001), IV (Istituto Nazionale di Geofisica e Vulcanologia, 2006), HU (Kövesligethy Radó Seismological Observatory, Geodetic And Geophysical Institute, Research Centre For Astronomy And Earth Sciences, Hungarian Academy Of Sciences, 1992), MN (MedNet Project Partner Institutions, 1990), ME (Institute of Hydrometeorology and Seismology of Montenegro, 1982), AC (Albanian seismic network, Institute of Geosciences, Polytechnic University of Tirana, 2002). We used the data from temporary stations installed within the AlpArray project (Z3, AlpArray Seismic Network, 2015). The data used in the research can be found at http://www.orfeus-eu.org/data/eida/ website or through request to the regional network operators. All support in collecting and storing seismic data is gratefully acknowledged. Operation of the stations CACV, KSY and STA is financed by the HEP group (Hrvatska elektroprivreda d.d.). The authors are grateful to the AlpArray Seismic Network Team who builds and maintains the entire AlpArray Seismic Network: György HETÉNYI, Rafael ABREU, Ivo ALLEGRETTI, Maria-Theresia APOLONER, Coralie AUBERT, Simon BESANÇON, Maxime BÈS DE BERC, Götz BOKELMANN, Didier BRUNEL, Marco CAPELLO, Martina ČARMAN, Adriano CAVALIERE, Jérôme CHÈZE, Claudio CHIARABBA, John CLINTON, Glenn COUGOULAT, Wayne C. CRAWFORD, Luigia CRISTIANO, Tibor CZIFRA, Ezio D'ALEMA, Stefania DANESI, Romuald DANIEL, Anke DANNOWSKI, Iva DASOVIĆ, Anne DESCHAMPS, Jean-Xavier DESSA, Cécile DOUBRE, Sven EGDORF, ETHZ-SED Electronics Lab, Tomislav FIKET, Kasper FISCHER, Wolfgang FRIEDERICH, Florian FUCHS, Sigward FUNKE, Domenico GIARDINI, Aladino GOVONI, Zoltán GRÁCZER, Gidera GRÖSCHL, Stefan HEIMERS, Ben HEIT, Davorka HERAK, Marijan HERAK, Johann HUBER, Dejan JARIĆ, Petr JEDLIČKA, Yan JIA, Hélène JUND, Edi KISSLING, Stefan KLINGEN, Bernhard KLOTZ, Petr KOLÍNSKÝ, Heidrun KOPP, Michael KORN, Josef KOTEK, Lothar KÜHNE, Krešo KUK, Dietrich LANGE, Jürgen LOOS, Sara LOVATI, Deny MALENGROS, Lucia MARGHERITI, Christophe MARON, Xavier MARTIN, Marco MASSA, Francesco MAZZARINI, Thomas MEIER, Laurent MÉTRAL, Irene MOLINARI, Milena MORETTI, Anna NARDI, Jurij PAHOR, Anne PAUL, Catherine PÉQUEGNAT, Daniel PETERSEN, Damiano PESARESI, Davide PICCININI, Claudia PIROMALLO, Thomas PLENEFISCH, Jaroslava PLOMEROVÁ, Silvia PONDRELLI, Snježan PREVOLNIK, Roman RACINE, Marc RÉGNIER, Miriam REISS, Joachim RITTER, Georg RÜMPKER, Simone SALIMBENI, Marco SANTULIN, Werner SCHERER, Sven SCHIPPKUS, Detlef SCHULTE-KORTNACK, Vesna ŠIPKA, Stefano SOLARINO, Daniele SPALLAROSSA, Kathrin SPIEKER, Josip STIPČEVIĆ, Angelo STROLLO, Bálint SÜLE, Gyöngyvér SZANYI, Eszter SZŰCS, Christine THOMAS, Martin THORWART, Frederik TILMANN, Stefan UEDING, Massimiliano VALLOCCHIA, Luděk VECSEY, René VOIGT, Joachim WASSERMANN, Zoltán WÉBER, Christian WEIDLE, Viktor WESZTERGOM, Gauthier WEYLAND, Stefan WIEMER, Felix WOLF, David WOLYNIEC, Thomas ZIEKE, Mladen ŽIVČIĆ, Helena ŽLEBČÍKOVÁ.

Appendix A

From Fig. 3 we see that the used Rayleigh waves (30 – 160 s) are dominantly sensitive to the upper mantle, which is also the main focus of this paper. However, every wavelength (period) has non-zero sensitivity to the uppermost layers as well. Even though the sensitivity is low and hence the resolution in the crust is poor, still the crustal structure has some influence on the inversion process. Improper velocities in the crust can bias the velocities in the upper mantle due to the tendency of the inversion to balance the possible extreme in one layer by the other extreme in the next layer. To evaluate the influence of the crustal structure on the depth inversion, we performed a test, where the crust has been fixed. While in the results shown in Figs. 5 – 8, the shear-wave velocity was found for all 23 layers above the halfspace as well as for the halfspace itself, in the test, we kept the uppermost 6 layers down to the depth of 35 km constant. Both V_s and V_p were taken from the average model of the whole studied region (used as the starting model, see above) and were not changed during the inversion.

Fig. A1 shows results of this inversion with fixed crust in comparison with the results of the inversion where the crust has been inverted for (varying crust). Similarly, as in Fig. 5, we now show two locations (blue stars on the left-hand side). The middle panels depict the local dispersion curves by blue dots with the dispersions corresponding to the final mean models obtained from 30 inversion runs. Right panels show the final mean models. Red lines are the results for the inversion as it was performed in our study above (varying crust), black lines are the results of the test with fixed crustal layers. In Fig. A1a, we see that the final models are very similar. Luckily, at this location, the inverted crustal structure (red) is very close to the average crustal structure (black) and hence also the upper mantle is represented with

almost the same model. The situation is different in Fig. A1b, where the inverted crust (red) resulted in significantly lower velocities than the fixed average (black). As in the testing inversion the crust was forced to be too fast (black), the layers immediately below the crust resulted in lower velocities than were those obtained during the original inversion (red). Too fast crust is balanced by too slow uppermost mantle. Also, there is an unrealistic negative step of velocities in the depth of 35 km. Below 90 km, the models are almost identical.

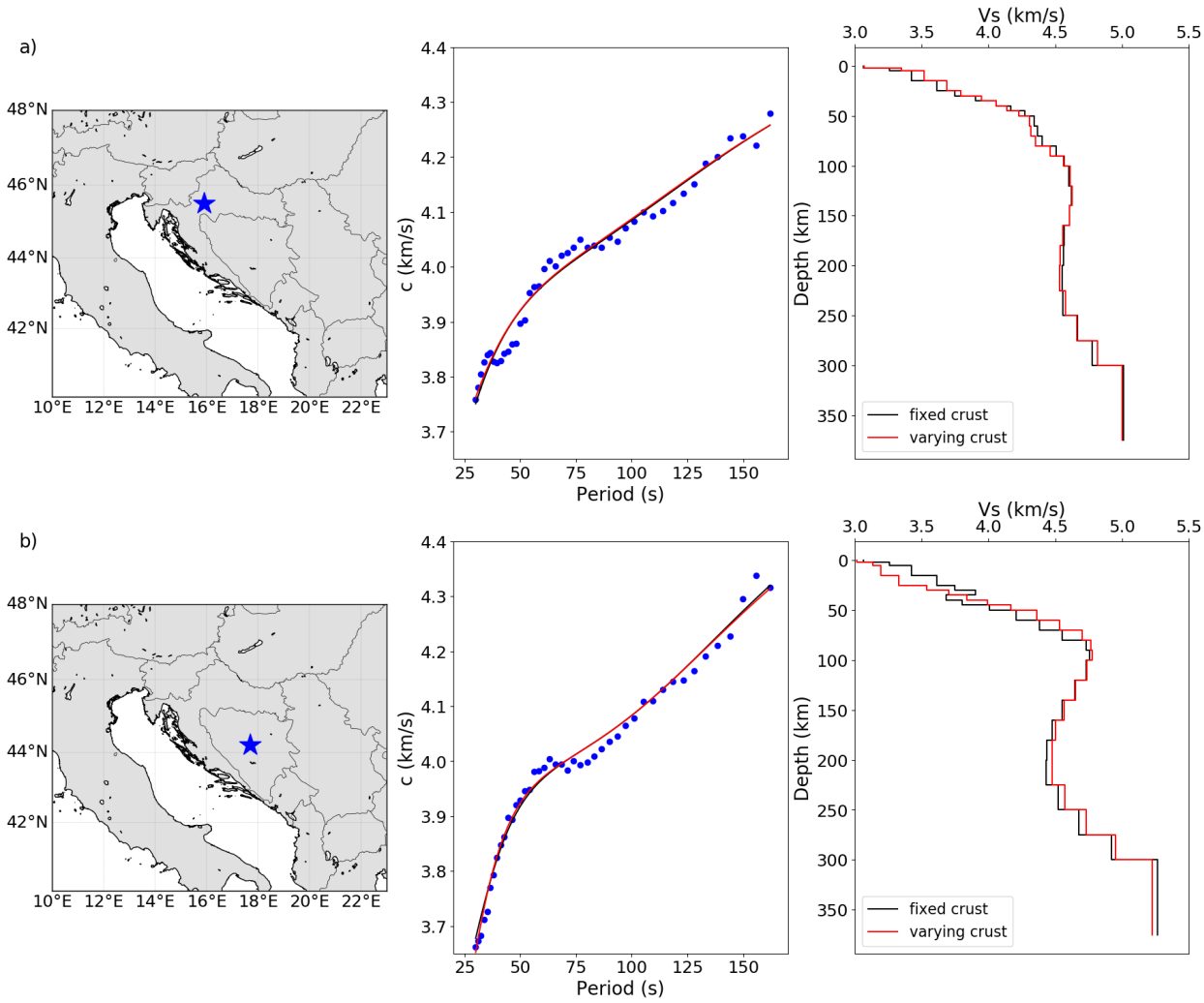

Figure A1: Examples of inverted velocity models with fixed and varying crust for two different locations. Star indicates location and blue dots show measured phase velocities. Red line is the dispersion curve of the final mean model with varying crust (similarly as in Fig. 5) and black one is for fixed crust.

The rightmost panel shows the final mean shear-wave velocity structure obtained after 30 inversions for varying (red line) and fixed crust (black line).

The differences between the models for varying and fixed crust can be evaluated quantitatively. We can compare the misfits of the dispersion curves corresponding to the final mean models. Misfit is defined here as the distance of the modeled curve from the measured one normalized by the number of measured points, so that we can compare the misfits even for curves with different number of measured points. In case of the example in Fig. A1a, the misfit of the curve for fixed crust is higher than the misfit of the curve for the varying crust by 0.007%, which is insignificant. For the case in Fig. A1b, it is 0.031%. This can be assessed also visually, as the red and black curves for both the examples are almost identical. Hence, misfit is not the measure, which evaluates the difference. Looking at the final mean models, we can define their complexity. Here we use an average of absolute values of all the velocity steps between the layers normalized by the number of layers. Higher complexity means the model is oscillating more. In case of Fig. A1a, the complexity of the fixed-crust model is lower by 1.8% compared to the model with varying crust. This is an interesting result. It means that keeping the crust fixed rises the misfit insignificantly and lowers the complexity a bit more. The product of the misfit and the complexity, which gives the distance of the model from the utopia point, is then lower for the fixed-crust example a). One could interpret this as that fixing the crust actually helped to achieve a better model. However, the situation is dramatically different for the other example, Fig. A1b. As we noted, the misfit is again a little bit higher for the fixed crust dispersion curve and the complexity of the corresponding final mean model is higher by 17%. It is mainly due to the oscillation right below the crust. Hence also the distance of the model from the utopia point is significantly higher. In this case, the varying-crust model is preferable.

Fig. A2 shows distributions of misfits (left panel) and complexities (right panel) for all the 4306 nodes for both varying and fixed crustal models. While the distribution of misfits is almost the same, there is a significant number of models with varying crust, which have lower complexity than the fixed-crust models. This is why we prefer models with varying crust.

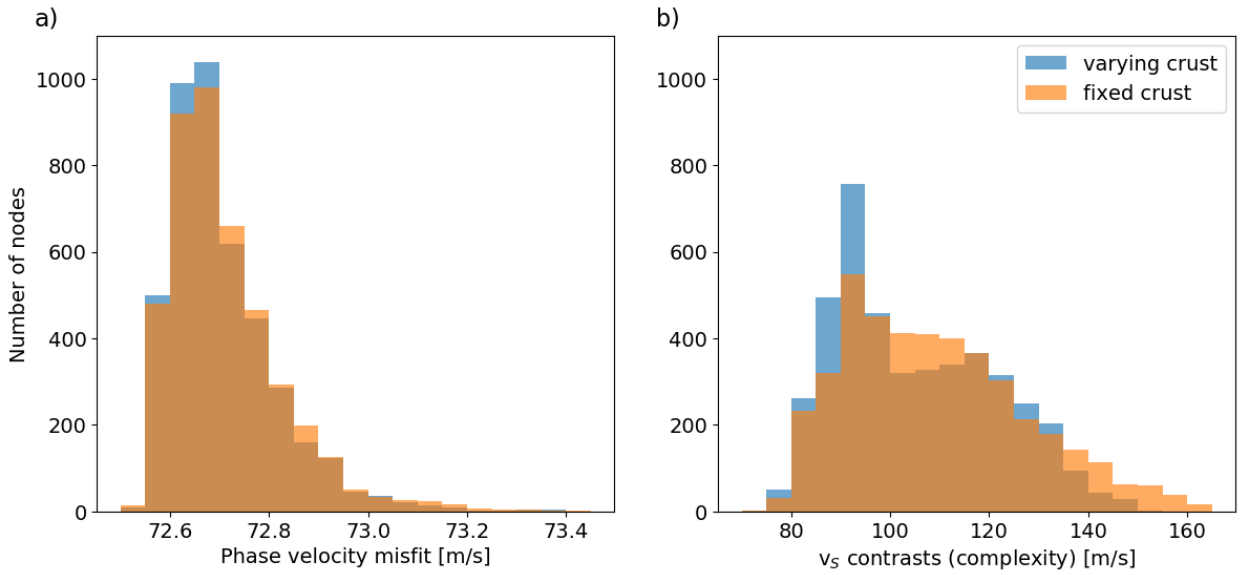

Figure A2: Distribution of misfits (a) and complexities (b) for all 4306 models. Blue columns in the background show the values for the models with varying crust, orange color in the front are the values for models with fixed crust.

Fig. A3 shows two cross-sections (JJ' and KK'). Left panels are for the original inversion with the varying crustal structure, right panels show the results for the upper mantle structure for the testing inversion with fixed crust. The uppermost parts down to the depth of 50 km are shown separately (different color scale) and the varying and fixed crust is clearly seen in these panels. Most important to notice here is, that even though the highest and the lowest velocities in the upper mantle differ slightly in their values (the maxima being a little bit more pronounced in the original inversion on the left, the minima being a little bit more

visible in the fixed inversion on the right), the overall upper mantle structure does not change. The anomalies stay at their positions in both cases. Even though both inversion schemes allow for the structural interpretation of the upper mantle, we consider the one with varying crust (used in the paper) more appropriate. This is due to the better fit to the data and because case with varying crust avoids unrealistic velocity contrasts and models are, in general, less complex.

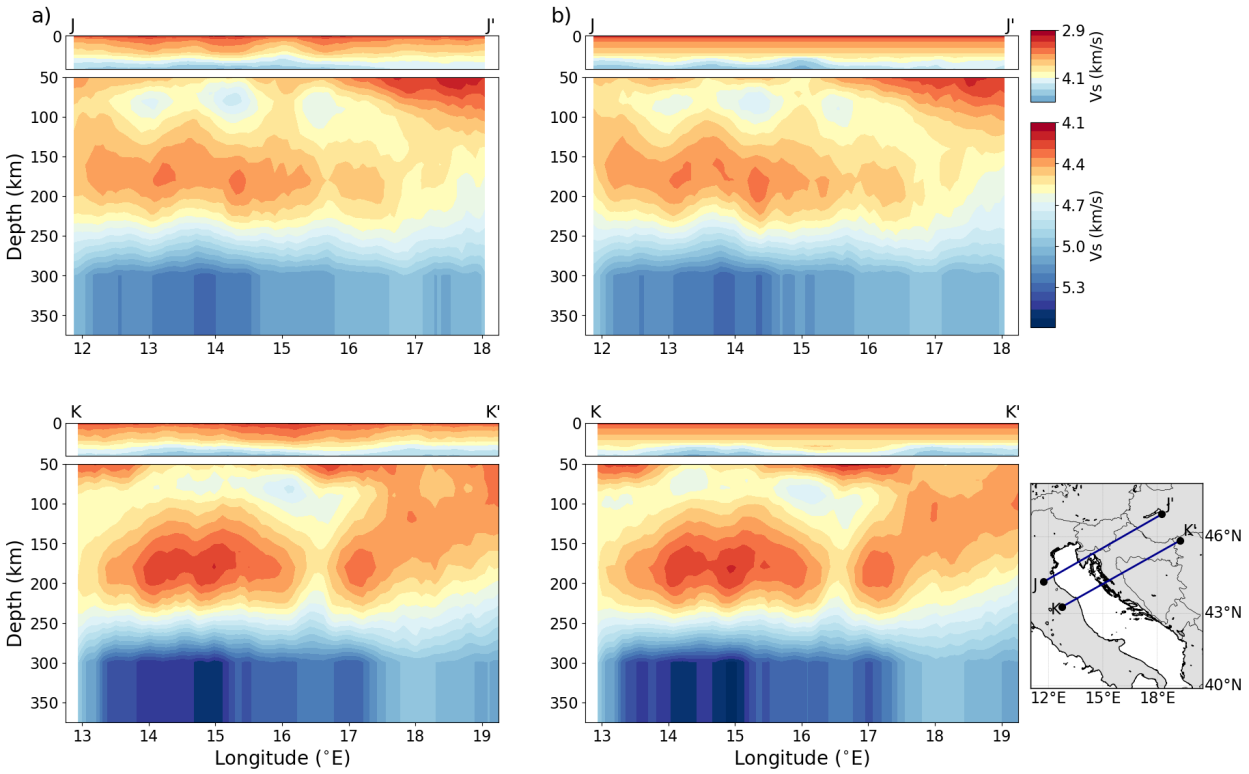

Figure A3: Two cross-sections of the shear wave velocity perpendicular to the orogen. Locations of profiles are displayed in the right corner. Inversion was done: a) with varying crust and b) fixed crust. The upper panel shows the structure of the crust and the lower one the structure of the upper mantle along the profile.

Appendix B

In Appendix A, we tested the influence of the crust on the inversion results in the upper mantle. For inversions both with varying and fixed crust, the deepest boundary was set to a

depth of 300 km with a halfspace below. The shear-wave velocity was still inverted for in the halfspace and hence we see lateral variations below 300 km (see the cross sections in Fig. 7). In addition, we performed tests, where we extended the depth by adding two more layers and shifting the last boundary of the halfspace to 410 km. In that case the layered model covers the whole upper mantle and the halfspace continues down to the transition zone. The inversion was performed the same way as before. We again took the density and v_P/v_S ratio from the ak132 model (Kennett et al., 1995). The starting model used was also the same as before in the first 23 layers. The original last velocity step at 300 km was split into three smaller steps for the new starting model in the depths of 300, 345 and 410 km. The aim was to investigate how the deeper parts of the upper mantle influence the results above 300 km. The sensitivities for all periods used are diminishing below 400 km, still, they are not zero.

Results are given in Fig. B1. Upper plots are equivalent to Fig. 5 and Fig. A1. As an example, we show one local dispersion curve (left plot, blue dots) and its corresponding models (right plot). The location of that model is shown in the map inset. Red line in the right plot is the shear wave distribution for the original inversion with the halfspace top at 300 km depth, and the green line shows the extended structure with the halfspace top at 410 km depth. The results are the same down to the original halfspace top at 300 km. Below, the additional two layers smeared the original velocity step into three smaller steps. This is typical behavior of dispersion curve inversion. If more layers are prescribed, the former velocity contrast is smeared over a larger range of depths.

The bottom plots show the cross-sections along the profile JJ' which is situated in between the profiles BB' and CC'. The left panel shows the results for the original inversion, similarly as in Fig. 7. The right panel in Fig. B1 shows the results for the same cross-section with halfspace at 410 km. The behavior shown for the 1D model is preserved along the whole cross-section. The former velocity contrast at the halfspace top is now smeared into the depth. The lateral variations are preserved. In other words, the additional layers do not show any new structural variations, only the former contrast between the last layer and the halfspace is now distributed to greater depths. The image in the top 300 km remains the same implying that the additional layers do not influence the results above 300 km.

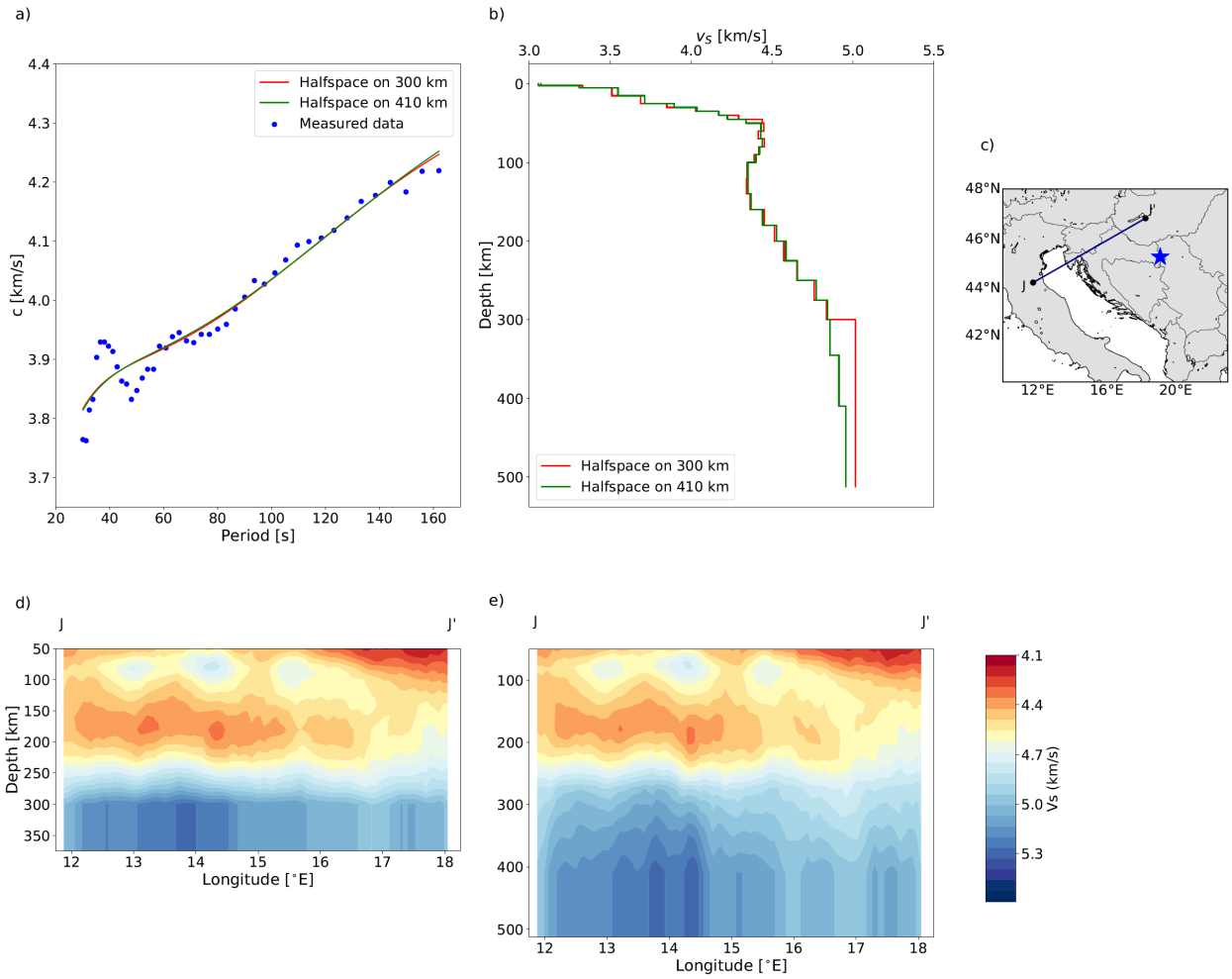

Figure B1: Upper left panel shows the local dispersion curve (blue dots) with the modeled dispersions for the final models of the two inversions. Red curve corresponds to the model with halfspace at 300 km and green curve to a model with the halfspace at 410 km. The respective models are given in the upper right plot. Bottom cross-sections follow the JJ' profile (map inset on the right). The left plot shows the results for halfspace at 300 km and the right one for halfspace at 410 km.

References

Anderson, H., Jackson, J., 1987. Active tectonics of the Adriatic region. Geophys. J. Int. 91, 937–983. https://doi.org/10.1111/j.1365-246X.1987.tb01675.x.

Aljinović, B., 1983. Najdublji seizmički horizonti sjeveroistočnog Jadrana. Doctoral dissertation (in Croatian). University of Zagreb, Faculty of Science.

Bartzsch, S., Lebedev, S., Meier, T., 2011. Resolving the lithosphere–asthenosphere boundary with seismic Rayleigh waves, Geophys. J. Int. 186,1152–1164. https://doi.org/10.1111/j.1365-246X.2011.05096.x.

Belinić, T., Stipčević, J., Živčić, M., 2018. Lithospheric thickness under the Dinarides. Earth. Planet. Sc. Lett. 484, 229–240. https://doi.org/10.1016/j.epsl.2017.12.030.

Bennett, R.A., Hreinsdóttir,, S., Buble, G., Baši, T., Bačić, Ž., Marjanović, M., Casale, G., Gendaszek, A., Cowan, D., 2008. Eocene to present subduction of southern Adria mantle lithosphere beneath the Dinarides. Geology 36, 3–6. https://doi.org/10.1130/G24136A.1.

Bijwaard, H., Spakman, W., 2000. Non-linear global P-wave tomography by iterated linearized inversion. Geophys. J. Int. 141, 71–82. https://doi.org/10.1046/j.1365-246X.2000.00053.x.

Bourova, E., Kassaras, I., Pedersen, H. A., Yanovskaya, T., Hatzfeld, D. and Kiratzi, A., 2005. Constraints on absolute S velocities beneath the Aegean Sea from surface wave analysis. Geophys. J. Int. 160, 1006–1019. https://doi.org/10.1111/j.1365-246X.2005.02565.x.

Brückl, E., Behm, M., Decker, K., Grad, M., Guterch, A., Keller, G.R., Thybo, H., 2010. Crustal structure and active tectonics in the Eastern Alps. Tectonics 29. https://doi.org/10.1029/2009TC002491.

Fang, L., Wu, J., Ding, Z. and Panza, G. F., 2010. High resolution Rayleigh wave group velocity tomography in North China from ambient seismic noise, Geophys. J. Int., 181, 1171–1182. https://doi.org/10.1111/j.1365-246X.2010.04571.x.

Foster, A., Ekström, G., Nettles, M., 2014. Surface wave phase velocities of the Western United States from a two-station method. Geophys. J. Int. 196, 1189–1206. https://doi.org/10.1093/gji/ggt454.

Frisch, W., Kuhlemann, J., Dunkl, I., Brügel, A., 1998. Palinspastic reconstruction and topographic evolution of the Eastern Alps during late Tertiary tectonic extrusion. Tectonophysics 297, 1–15. https://doi.org/10.1016/S0040-1951(98)00160-7.

Grenerczy, G., Sella, G., Stein, S., Kenyeres, A., 2005. Tectonic implications of the GPS velocity eld in the northern Adriatic region. Geophys. Res. Lett. 32, L16311. https://doi.org/10.1029/2005GL022947.

Guidarelli, M., Aoudia, A., Costa, G., 2017. 3-D structure of the crust and uppermost mantle at the junction between the Southeastern Alps and External Dinarides from ambient noise tomography. Geophys. J. Int. 211, 1509–1523. https://doi.org/10.1093/gji/ggx379.

van Hinsbergen, D.J.J., Torsvik, T.H., Schmid, S.M., Maţenco, L.C., Maffione, M., Vissers, R.L.M., Gürer, D. and Spakman, W., 2019. Orogenic architecture of the Mediterranean region and kinematic reconstruction of its tectonic evolution since the Triassic. Gondwana Res. 81, 79–229. https://doi.org/10.1016/ j.gr.2019.07.009.

Handy, M.R., Giese, J., Schmid, S.M., Pleuger, J., Spakman, W., Onuzi, K., Ustaszewski, K., 2019. Coupled crust-mantle response to slab tearing, bending, and rollback along the Dinaride-Hellenide orogen. Tectonics 38, 2803–2828.https://doi.org/10.1029/2019TC005524.

Handy, M.R., Ustaszewski, K., Kissling, E., 2015. Reconstructing the Alps–Carpathians–Dinarides as a key to understanding switches in subduction polarity, slab gaps and surface motion. Int. J. Earth. Sci. 104, 1–26. https://doi.org/10.1007/s00531-014-1060-3.

Herrmann, R.B., 2013. Computer programs in seismology: An evolving tool for instruction and research. Seism. Res. Lettr. 84, 1081–1088. https://doi.org/10.1785/0220110096.

Horváth, F., Bada, G., Szafián P., Tari, G., Ádám,, A., Cloetingh, S., 2006. Formation and deformation of the Pannonian Basin: Constraints from observational data. Geol. Soc. Mem. 32, 191–206. https://doi.org/10.1144/GSL.MEM.2006.032.01.11.

Kästle, E. D., El-Sharkawy, A., Boschi, L., Meier, T., Rosenberg, C., Bellahsen, N., Weidle, C., 2018. Surface wave tomography of the Alps using ambient-noise and earthquake phase velocity measurements, J. Geophy. Res: Solid Earth, 123, 1770–1792. https://doi.org/10.1002/2017JB014698.

Kästle, E. D., Rosenberg, C., Boschi, L., Bellahsen, N., Meier, T., and El-Sharkawy, A., 2020. Slab break-offs in the Alpine subduction zone, Int. J. Earth. Sci., 109, 587–603, https://doi.org/10.1007/s00531-020-01821-z.

Kennett, B.L.N., Engdahl, E.R., Buland, R., 1995. Constraints on seismic velocities in the Earth from travel times. Geophys. J. Int. 122, 108–124. https://doi.org/10.1111/j.1365-246X.1995.tb03540.x.

Kolínský, P., Málek, J., Brokešová, J., 2011. Shear wave crustal velocity model of the Western Bohemian Massif from Love wave phase velocity dispersion. J. Seismol. 15, 81–104. https://doi.org/10.1007/s10950-010-9209-4.

Kolínský, P., Valenta, J., Málek, J., 2014. Velocity model of the Hronov-Poříčí Fault Zone from Rayleigh wave dispersion, J. Seismol. 18, 617–635. https://doi.org/10.1007/s10950-014-9433-4.

Koulakov, I., Kaban, M.K., Tesauro, M., Cloetingh, S., 2009. P- and S-velocity anomalies in the upper mantle beneath Europe from tomographic inversion of ISC data. Geophys. J. Int. 179, 345–366. https://doi.org/10.1111/j.1365-246X.2009.04279.x.

Lippitsch, R., Kissling, E., Ansorge, J., 2003. Upper mantle structure beneath the Alpine orogen from high-resolution teleseismic tomography. J. Geophys. Res. Solid Earth 108, 2376https://doi.org/10.1029/2002JB002016.

Matenco, L., Radivojević, D., 2012. On the formation and evolution of the Pannonian Basin: Constraints derived from the structure of the junction area between the Carpathians and Dinarides. Tectonics 31. https://doi.org/10.10292012TC003206.

Málek, J., Růžek, B., Kolář, P., 2007. Isometric method: Efficient tool for solving non-linear inverse problems. Stud. Geophys. Geod. 51, 469–490. https://doi.org/10.1007/s11200-007-0028-1.

Mitterbauer, U., Behm, M., Brückl, E., Lippitsch, R., Guterch, A., Keller, G.R., Koslovskaya, E., Rumpfhuber, E.M., Šumanovac, F., 2011. Shape and origin of the East-Alpine slab

constrained by the ALPASS teleseismic model. Tectonophysics 510, 195–206. https://doi.org/10.1016/j.tecto.2011.07.001.

Molinari, I., Clinton, J., Kissling, E., Hetényi, G., Giardini, D., Stipčević, J., Dasović, I., Herak, M., Šipka, V., Weéber, Z., Gráczer, Z., Solarino, S., the Swiss–AlpArray Field Team, the AlpArray Working Group, 2016. Swiss-alparray temporary broadband seismic stations deployment and noise characterization. Adv. Geosci. 43, 15–29. https://doi.org/10.5194/adgeo-43-15-2016.

Pamić, J., Gušić, I., Jelaska, V., 1998. Geodynamic evolution of the Central Dinarides. Tectonophysics 297, 251–268. https://doi.org/10.1016/S0040-1951(98)00171-1.

Panza, G. F., Raykova, R. B., Carminati, E. and Doglioni, C., 2007. Upper mantle flow in the western Mediterranean, Earth and Planetary Science Letters 257, 200–214. https://doi.org/10.1016/j.epsl.2007.02.032.

Piromallo, C., Morelli, A., 2003. P wave tomography of the mantle under the Alpine-Mediterranean area. J. Geophys. Res. Solid Earth 108, 2065. https://doi.org/10.1029/2002JB001757.

Raykova, R., Nikolova, S., 2007. Tomography and velocity structure of the crust and uppermost mantle in southeastern Europe obtained from surface wave analysis. Stud. Geophys. Geod. 51, 165–184. https://doi.org/10.1007/s11200-007-0008-5.

Ritzwoller, H. M., Levshin A. L., 1998. Eurasian surface wave tomography: group velocities.J. Geophys. Res. 103, 4839–4878. https://doi.org/10.1029/97JB02622.

Royden, L., Horváth, F., 1988. The Pannonian Basin: A study in basin evolution. AAPG Memoirs 45.. https://doi.org/10.1306/M45474.

Schefer, S., Cvetković, V., Fügenschuh, B., Kounov, A., Ovtcharova, M., Schaltegger, U., Schmid, S.M., 2011. Cenozoic granitoids in the Dinarides of southern Serbia: age of intrusion, isotope geochemistry, exhumation history and significance for the geodynamic evolution of the Balkan Peninsula. Int. J. Earth Sci. 100, 1181–1206. https://doi.org/10.1007/s00531-010-0599-x.

Schmid, S. M., Bernoulli, D., Fügenschuh, B., Matenco, L., Schefer, S., Schuster, R., Tischler, M., Ustaszewski, K., 2008. The Alpine-Carpathian-Dinaridic orogenic system: correlation and evolution of tectonic units. Swiss J. Geosci. 101, 1, 139–183. https://doi.org/10.1007/s00015-008-1247-3.

Schmid, S.M., Fügenschuh, B., Kounov, A., Matenco, L, Nievergelt, P., Oberhänsli, R., Pleuger, J., Schefer, S., Schuster, R., Tomljenović, B., Ustaszewski, K., Van Hinsbergen, D.J.J., 2020. Tectonic units of the Alpine collision zone between Eastern Alps and western Turkey, Gondwana Res. 78, 308–374. https://doi.org/10.1016/j.gr.2019.07.005.

Stipčević, J., Tkalčić, H., Herak, M., Markušić, S., Herak, D., 2011. Crustal and uppermost mantle structure beneath the External Dinarides, Croatia, determined from teleseismic receiver functions. Geophys. J. Int. 185, 1103–1119. https://doi.org/10.1111/j.1365-246X.2011.05004.x.

Šumanovac, F., 2015. Lithosphere model of the Pannonian-Adriatic overthrusting. Tectonophysics 665, 79–91. https://doi.org/10.1016/j.tecto.2015.09.032.

Šumanovac, F., Dudjak, D., 2016. Descending lithosphere slab beneath the northwest Dinarides from teleseismic tomography. J. Geodyn. 102, 171–184. https://doi.org/10.1016/j.jog.2016.09.007.

Šumanovac, F., Markušić, S., Engelsfeld, T., Jurković, K., Orešković, J., 2017. Shallow and deep lithosphere slabs beneath the Dinarides from teleseismic tomography as the result of the Adriatic lithosphere downwelling. Tectonophysics 712-713, 523–541. https://doi.org/10.1016/j.tecto.2017.06.018.

Šumanovac, F., Orešković, J., Grad, M., 2009. Crustal structure at the contact of the Dinarides and Pannonian basin based on 2-D seismic and gravity interpretation of the Alp07 prole in the ALP 2002 experiment. Geophys. J. Int. 179, 615–633. https://doi.org/10.1111/j.1365-246X.2009.04288.x.

Tari, V., 2002. Evolution of the northern and western Dinarides: a tectonostratigraphic approach. EGU Stephan Mueller Special Publication Series 1.

Tondi, R., Vuan, A., Borghi, A,. Argnani, A., 2019. Integrated crustal model beneath the Po Plain (Northern Italy) from surface wave tomography and Bouguer gravity data, Tectonophysics, 750, 262–279. https://doi.org/10.1016/j.tecto.2018.10.018.

van Unen, M., Matenco, L., Nader, F. H., Darnault, R., Mandic, O., Demir, V. (2019). Kinematics of foreland-vergent crustal accretion: Inferences from the Dinarides evolution. Tectonics 38, 49–76. https://doi.org/10.1029/2018TC005066.

Ustaszewski, K., Kounov, A., Schmid, S.M., Schaltegger, U., Krenn, E., Frank, W., Fügenschuh, B., 2010. Evolution of the Adria-Europe plate boundary in the northern Dinarides: From continent-continent collision to back-arc extension. Tectonics 29, TC6017, https://doi.org/10.1029/2010TC002668.

Ustaszewski, K., Schmid, S.M., Fugenschuh, B., Tischler, M., Kissling, E., Spakman, W., 2008. A map-view restoration of the Alpine-Carpathian- Dinaridic system for the Early Miocene. Swiss J. Geosci. 101, 273–294. https://doi.org/10.1007/s00015-008-1288-7.

Vlahović, I., Tišljar, J., Velić, I., Matičec, D., 2005. Evolution of the Adriatic Carbonate Platform: Palaeogeography, main events and depositional dynamics. Palaeogeogr. Palaeocl. 220, 333–360. https://doi.org/10.1016/j.palaeo.2005.01.011.

Vrabec, M., Prešeren, P., Stopar, B., 2006. GPS study (1996-2002) of active deformation along the Periadriatic fault system in northeastern Slovenia: tectonic model. Geol. Carpath. 57, 57–65.

Wortel, M.J.R., Spakman, W., 2000. Subduction and slab detachment in the Mediterranean-Carpathian region. Science 290, 1910–1917. https://doi.org/10.1126/Science.290.5498.1910.

Yanovskaya, T.B., Ditmar, P.G., 1990. Smoothness criteria in surface wave tomography. Geophys. J. Int. 102, 63–72. https://doi.org/10.1111/j.1365-246X.1990.tb00530.x.

Yanovskaya, T.B., Kizima, E.S., Antonova, L.M., 1998. Structure of the crust in the Black Sea and adjoining regions from surface wave data. J. Seismol., **2**, 303–316 https://doi.org/10.1023/A:1009716017960.

Yao, H., van Der Hilst, R.D., de Hoop, M.V., 2006. Surface-wave array tomography in SE Tibet from ambient seismic noise and two-station analysis: I. Phase velocity maps. Geophys. J. Int. 166, 732–744. https://doi.org/10.1111/j.1365-246X.2006.03028.x.

Zhu, H., Bozdağ, E., Peter, D., Tromp, J., 2012. Structure of the European upper mantle revealed by adjoint tomography. Nat. Geosci. 5, 493–498. https://doi.org/10.1038/ngeo1501.

ANSS - U.S. Geological Survey, Earthquake Hazards Program (2017) Advanced National Seismic System (ANSS) Comprehensive Catalog of Earthquake Events and Products: Various, https://doi.org/10.5066/F7MS3QZH.

Z3 - AlpArray Seismic Network. (2015). AlpArray Seismic Network (AASN) temporary component. AlpArray Working Group. https://doi.org/10.12686/alparray/z3_2015.

SL - Slovenian Environment Agency (2001): Seismic Network of the Republic of Slovenia. International Federation of Digital Seismograph Networks. Other/Seismic Network. 10.7914/SN/SL.

IV - INGV Seismological Data Centre. (2006, January 1). Rete Sismica Nazionale (RSN). Istituto Nazionale di Geofisica e Vulcanologia (INGV), Italy. https://doi.org/10.13127/sd/x0fxnh7qfy.

HU - Kövesligethy Radó Seismological Observatory (Geodetic And Geophysical Institute, Research Centre For Astronomy And Earth Sciences, Hungarian Academy Of Sciences (MTA CSFK GGI KRSZO)). (1992). Hungarian National Seismological Network. Deutsches GeoForschungsZentrum GFZ. https://doi.org/10.14470/uh028726.

MN - MedNet Project Partner Institutions. (1990, January 1). Mediterranean Very Broadband Seismographic Network (MedNet). Istituto Nazionale di Geofisica e Vulcanologia (INGV), Italy. https://doi.org/10.13127/sd/fbbbtdtd6q.

ME - Sector for Seismology, Institute of Hydrometeorology and Seismology of Montenegro (1982): Montenegrin Seismic Network. Sector for Seismology, Institute of Hydrometeorology and Seismology of Montenegro. Dataset/Seismic Network. 10.7914/SN/ME.

AC - Institute of Geosciences, Energy, Water and Environment (2002): Albanian Seismological Network. International Federation of Digital Seismograph Networks. Dataset/Seismic Network. 10.7914/SN/AC.